JOINT EUROPEAN TORUS

JET–P(91)43

P.A. Duperrex, A. Pochelon, A. Edwards, J Snipes
and JET Team

Global Sawtooth Instability Measured by Magnetic Coils in the JET Tokamak

Global Sawtooth Instability Measured by Magnetic Coils in the JET Tokamak

P.A. Duperrex[1,3], A. Pochelon[1], A. Edwards, J Snipes[2]
and JET Team*

JET-Joint Undertaking, Culham Science Centre, OX14 3DB, Abingdon, UK

[1]Centre de Recerches en Physique des Plasmas/EPFL, Lausanne, Switzerland.
[2]MIT Plasma Fusion Center, Cambridge, MA, USA.
[3]Defence Technology and Procurement Agency, Bern, Switzerland
** See Appendix 1*

Preprint of Paper to be submitted for publication in
Nuclear Fusion

GLOBAL SAWTOOTH INSTABILITY MEASURED BY MAGNETIC COILS IN THE JET TOKAMAK

P.A. Duperrex[1*], A. Pochelon[1], A. Edwards, J. Snipes[2].

JET Joint Undertaking
Abingdon, Oxfordshire OX14 3EA
Great Britain

ABSTRACT

This paper describes measurements of the sawtooth instability in JET, in which the instability wave function is shown to extend to the edge where it is measured using magnetic coils. The numerous magnetic probes in JET allow the time evolution of the (n=0, 1, 2, 3) toroidal Fourier components to be analysed. The n=1 magnetic component is measured to be similar to the m=1 soft X-ray centroid motion. This fact indicates the potential of edge signals in retrieving the poloidal mode spectrum of the q=m/n=1 surface. The spectrum evolution of the instability is compared for normal sawteeth (NST) and quasi-stabilised "monster" sawteeth (MST). The spectrum is slowly decreasing with n for NST and all the components belong to one ballooning-like deformation, whereas MST show a large n=1 kink-like motion with small and independent accompanying higher n modes. Important equilibrium changes are measured to occur already during the growth of the instability and the growth rate is much faster than exponential, both facts implying the non-linear nature of the instability growth. Parametric dependence of growthrates, amplitudes, toroidal spectrum shape, etc., are studied to characterize the NST and MST instability.

1) Permanent address: Centre de Recherches en Physique des Plasmas/EPFL, 21, Av. des Bains, CH-1007 Lausanne, Switzerland
2) Permanent address: MIT Plasma Fusion Center, 175 Albany St., Cambridge, MA 02139, USA
* Present address: Defence Technology and Procurement Agency, 65 Stauffacherstr. CH-3000 Bern, Switzerland

I INTRODUCTION

Though sawtooth instabilities have been observed in tokamaks and studied for many years [1], the understanding of their mechanism still represents a challenge for the tokamak community and the experiments continue to regularly reveal new surprises. A strong motivation for studying these internal disruptions lies in the hope of stabilizing the sawtooth relaxations in a reactor. These represent a serious central performance limiting factor by periodically ejecting the hot central plasma and fast particles. Experimental successes have already been obtained in extending the sawtooth duration over several global energy confinement times and thereby appreciably improving central parameters (JET's so-called monster sawteeth [2]), typically gaining a factor of two on the fusion yield. The definitive understanding of the observed phenomena seems however to lag behind experimental achievements. Among the reasons responsible for this situation is certainly the difficulty in measuring the central current profile with the required precision. Fast particle populations are also expected to play an important role [3,4]. This all leads to a situation where the nature of the instability responsible for the sawtooth crash is not yet well known.

The aim of this paper is to present new and detailed experimental results about the sawtooth instability, based on measurements from magnetic pick-up coils located in the shadow of the limiters. Although we make use of edge signals to measure internal disruptions, it will be shown that magnetic coils represent a powerful tool to characterize sawtooth instabilities in a tight-aspect-ratio machine with elongation bigger than one such as JET. With the large number of coils available in JET (18 poloidal at 8 symetric toroidal locations), see Fig. 1, an efficient spatial and temporal description of the instability is possible. This gives access to the toroidal

mode number spectrum and its temporal evolution, the growth rates of the instability, etc. The good ability to obtain these values from magnetic coil measurements makes it possible to test and to establish various scaling laws on the sawtooth instability. This paper aims at the characterization of the sawtooth instability or the succession of instabilities leading to the sawtooth crash, also called internal disruption. The paper therefore concentrates on the rapid growth phase, a period representing typically 1 to 0.1 percent of the full sawtooth period in JET.

In the first sawtooth relaxation measurements using soft X-ray emission [1], the m=0, n=0 thermal relaxations were preceded by a growing m=n=1 helical perturbation localized at the estimated radius of the q=1 surface, and seen as a sinusoidal oscillation due to plasma rotation. The growth of this slow precursor oscillation was believed to be responsible for the sawtooth crash. The growth rate of this precursor was however an order of magnitude slower than the growth rate of the ideal internal kink mode [5]. Kadomtsev interpreted this precursor as an m=n=1 tearing mode growing to full invasion of the core volume encompassed by the island [6]. This picture was in apparent contradiction with the observation of an m=n=1 oscillation continuing after the sawtooth crash [7]. The comparison of experimental soft X-ray traces with simulated chord signals obtained by integrating over a soft X-ray emission model profile which contained a growing and rotating island, identified the slow growing oscillation with an island. This island could remain relatively small until the beginning of the fast sawtooth crash [8], which the simulation did not resolve. The rapidity of the sawtooth crash seemed to imply that a faster event than the island growth should be involved in the relaxation. The link between current profiles and sawtooth activity was investigated by polarimetry measurements [9]. Fast changes in the central safety factor on axis q(0) at the crash were also shown by these diagnostics [9,10] and by the use of

global Alfvén waves [11]. The measured current crash time was comparable in duration to the sawtooth crash time [11] which indicated that a convective current transport mechanism seemed to apply at the instability crash.

The fast character of the sawtooth crash in large tokamaks such as JET [12] or TFTR was puzzling. Analytical calculations showed that the ideal internal kink in toroidal geometry is stable below a critical β_p [13]. Toroidal geometry couples the m=1 internal mode to outer resonant surfaces, thereby extending the motion to larger radii, an effect further enhanced by inclusion of resistivity [14]. Concerning the growth rate, the addition of resistivity was shown to increase the growth rate over the ideal value [15]. Further inclusion of electron inertia [16,17] increased the growth rate to the values observed in large and small tokamaks .

In JET, an edge magnetic perturbation correlated with the sawtooth crash was detected with the magnetic pick-up coils [18] and was used to determine the sawtooth characteristics [19,20]. Earlier hints of a direct effect of the sawtooth instability on the plasma edge were observed in the T-10 tokamak where the tokamak liner exhibited arc tracks oriented along a direction corresponding to an m=1 n=1 mode, that is, oriented along q=1 [21]. The edge magnetic perturbation associated with the sawtooth crash is visible for all sawteeth in JET. In this paper, we make use of this edge magnetic perturbation in JET - which we have called the gong - and develop it to the level of a tool to characterize the internal disruption, or better said, to characterize different types of internal disruptions.

The paper is constructed as follows. In section II, we characterize the magnetic perturbation occurring at the sawtooth crash, and show how the toroidal mode number spectrum is obtained. With the help of soft X-ray data, we demonstrate in section III that edge magnetic measurements represent adequately the internal disruption, or sawtooth instability. In the

following section IV, we discuss the significance of the toroidal mode number spectrum obtained and we compare spectra from normal sawteeth (NST) and from stabilized sawteeth, the so-called "monster" sawteeth (MST). The magnetic sawtooth instability data are then used in section V to determine scaling laws for the internal disruption instability. The results are discussed in section VI and the conclusions are presented in section VII.

I I SPATIAL AND TEMPORAL CHARACTERISTICS OF THE GONG

The sawtooth instability in tokamaks is usually studied using core data such as the electron temperature or density, that is by following soft X-ray, electron cyclotron emission or interferometric measurements. In the JET tokamak each sawtooth is accompanied by a marked poloidal magnetic field perturbation at the wall. When this magnetic perturbation first was observed [18,19], it was named the "gong perturbation", suggested by the analogy of a gong being hit in its centre by a hammer - the sawtooth instability - and thus being brought into vibration up to the edge. It is interesting to mention that magnetic activity equivalent to the gong had not been reported earlier in smaller machines [22]. On the other hand, the fact that the gong can be observed easily on large machines of a similar aspect ratio to JET (R/a=2.5), such as TFTR (with R/a=2.9) [23] and DIII-D (with R/a=2.5) [24] suggests that mode coupling in tight aspect ratio tokamaks may be responsible for allowing the mode to be observed at the wall.

This chapter reports on measurements of the spatial properties of the sawtooth instability, Fourier analysing edge magnetic perturbations in the toroidal and poloidal directions. The measured poloidal mode number

structure results from toroidal coupling effects. Fast equilibrium changes will be shown to be already important prior to the sawtooth crash, that is during the instability growth.

The gongs observed on the magnetic pick-up coils show the same repetition frequency as the sawtooth activity measured on the soft X-rays, Fig. 2. Their level is well above the level of background oscillations and magnetic turbulence. The increase of the H_α signal, which is indicative of the heat pulse released by the internal disruption and reaching the edge, starts only some tens of milliseconds after the central temperature has dropped. The fast events observed in the core with the soft X-ray diodes and at the edge with the magnetic coils are perfectly correlated in time as is shown in Fig. 3 : to each peak on the soft X-ray signal there is a corresponding magnetic counterpart $\tilde{b}_\theta$. To avoid any possible instrumental timing lag, the different signals are recorded on the same ADC. The soft X-ray diode signal shown in the figure views the plasma slightly inside the sawtooth inversion radius, from where the first visible events of the sawtooth instability on the soft X-ray emission profiles are always observed.

It must be noted from the beginning that this so-called gong activity appears to be essentially different from Mirnov or island activity which is often observed to be modulated by the sawtooth activity, especially in low $q_\psi(a)$ discharges. Before fully establishing this point, it can already be mentioned that the gong appears in JET always as a fast transient pulse of short duration (~100μs), whereas the ongoing Mirnov activity presents an oscillatory character extending over many periods and showing a great variety of different (n,m) combinations, with various possible precursor and successor sequences around the sawtooth crash. Figure 4 shows an example of a gong taking place during Mirnov activity. The fast sampling frequency allows the two different phenomena to be separated by observing

the sudden change occurring in the magnetic activity, with an abrupt jump in amplitude, phase and frequency, while the oscillating mode continues with no change in phase. In the JET tokamak, the gong is much faster than the slow Mirnov rotation and develops typically in a tenth of a toroidal rotation period in ohmic discharges. This enables the two oscillation types to be clearly distinguished, already on the basis of the raw magnetic coil traces. Such a simple distinction is more difficult in a discharge with a large toroidal rotation velocity like, for example, in the case of neutral beam heating in the TFTR tokamak [23], where the sawtooth instability, and therefore the corresponding gong, develops over more than a Mirnov rotation period. Most frequently in JET ohmic discharges there are no slow oscillations before the sawtooth instability usually described as the (slow) precursor oscillations. The possible absence of any precursor was already reported for earlier smaller tokamaks, especially for high density discharges [25,26].

The experimental set-up and typical discharge conditions used in the present study are now described. The $\tilde{b}_\theta$ probes layout is depicted in Fig. 1 for one of the eight equi-spaced octants. A 10 KHz high frequency cut-off (-3dB) of the pick-up coils is fixed by the 2.5mm thick protective inconel casing of the coils. This nevertheless allows signals to be measured up to 60 - 80 kHz [27]. The time scale of the oscillations studied in this paper (50μs - 1ms) is therefore well covered by the measuring coils. The time scale of these oscillations is on the other hand short compared to the vacuum vessel penetration time, which is typically 4 ms for a transverse field [28]. The vessel can therefore be considered nearly an ideal conductor when compared to the sawtooth crash time scale. For the presented data, the acquisition sampling rate was 40kHz giving 25μs time resolution.

The sawteeth analyzed in this paper cover a large range of discharge geometries with major radius $R \cong 2.96$ m, minor radius $a = 1.25$ m, aspect

ratio 2.4 < R/a < 2.6, and plasma elongation 1.3 < b/a < 1.7. The data were collected from ohmic and auxiliary heated discharges (B_φ < 3.4T, Ip < 6MA) with a broad range of edge safety factors 2 < $q_\psi(a)$ < 10. The auxiliary heating was mainly Ion Cyclotron Resonance Heating (ICRH) (PRF < 10MW) though some data with Neutral Beam Injection (NBI) (PNBI < 10MW) or combined heating have also been included. Electron temperatures in the 2 - 4 KeV range in ohmic conditions may reach the 8 KeV range with additional heating, increasing the sawtooth relative electron temperature drop ΔTe/Te from 10 - 20 % in ohmic conditions up to 50 % with auxiliary heating. But more dramatically, the use of appropriate additional heating has allowed the sawtooth period to be prolonged from a few hundreds of milliseconds to several seconds. These "monster" sawteeth permit higher asymptotic central parameters to be achieved and the global confinement time to be increased [2]. Both normal sawteeth (NST) and monster sawteeth (MST) are analyzed in this paper.

The spatial characteristics of the gong are easily deduced by using the large number of $\tilde{b}_\theta$ pick-up coils available in JET. These coils, regularly distributed over the surface of the vessel, allow us to perform toroidal and poloidal mode number analysis, to measure in-out asymmetries and to deduce the helicity of the gong instability.

For the toroidal analysis, we use N=8 pick-up coils all at the same poloidal location and toroidally separated by 45°. The standard measurements used the coils poloidally located on the low field side (LFS) due to their larger signals (usually coil 3, see Fig. 1), and also to avoid increased response delays due to additional mechanical elements placed in the vessel in front of some of the more equatorial probes, such as coil 1). This allows the n=0, 1, 2, 3 and cos(4ϕ) Fourier components to be measured (or n=0, 1 and cos(2ϕ) if only 4 coils are used).

The different cosine and sine components are defined as follows :

for the n=0 component:

$$c_{n=0} = \frac{1}{N} \sum_{i=1}^{N} \tilde{b}_\theta(\varphi_i)$$

$$s_{n=0} = 0$$

and for the higher n components :

$$c_{n>0} = \frac{2}{N} \sum_{i=1}^{N} \tilde{b}_\theta(\varphi_i) \cdot \cos(n \cdot \varphi_i)$$

$$s_{n>0} = \frac{2}{N} \sum_{i=1}^{N} \tilde{b}_\theta(\varphi_i) \cdot \sin(n \cdot \varphi_i) \qquad (1a)$$

where $\tilde{b}_\theta(\varphi_i)$ are the integrated pick-up coil signals relative to the toroidal angles $\varphi_i = i \cdot \frac{2\pi}{N}$. The module is then :

$$b_n = \sqrt{c_n^2 + s_n^2}$$

and the toroidal phase :

$$\phi_n = \text{arc tg}(s_n / c_n)$$

All of the following analysis uses integrated probe signals $\tilde{b}_\theta(\varphi_i) = \int \dot{\tilde{b}}_\theta(\varphi_i) \cdot dt$, unless otherwise specified.

The time dependence of the different n-components contains important information on the nature of the instability. As an example, the time evolution of the different components in the case of a normal sawtooth is shown in Fig. 5. The n=0, 1, 2, 3 (and cos(4 ϕ)) spectrum components are calculated from the 8 integrated coil signals, shown on the lower traces. The time t_o has been arbitrarily defined by the time when the unintegrated n=1 component $\dot{b}_{\theta\, n=1}$ is maximum and the higher n components grow more

or less in parallel. The n=1 component develops typically in 100 to 500μs before it reaches saturation. The n=1 component, in the range of a few 10^{-4}T for normal sawteeth, is clearly the dominant toroidal mode number, though the n=2 component is non negligible and represents typically 25% of the n=1 component at saturation. The spectrum shows a rapid decrease towards higher n's. This suggests that the 8 coils used for the toroidal mode number analysis should be sufficient to describe adequately the spectrum, if the spectrum really continues to decrease monotonically at the higher n's, as it appears from the n<4 components. This is verified in particular when the number of coils used for the analysis is decreased from 8 coils to 4 coils, the absolute n=1 amplitude is only changed by ~10^{-3}. This confirms that the motion is dominated by the n=1 component, and does not contain important n>2 contributions. The example in Fig. 6 shows that the n=1, 2, 3 components grow approximately in parallel (i.e. spectrum shape unchanged). At their saturation the higher n's exhibit a small lag . The n'th amplitude maxima are indeed systematically delayed by a few tens of microseconds as compared to the (n-1)th maxima. In other words, the spectrum shape spreads out at saturation.

The n=0 component, which represents the Shafranov shift, starts its motion at the same time as the other components, has its maximum growth rate while the other components are saturating, and saturates while the n≥1 instability components have vanished. The n=0 corresponds to a global radial displacement towards the high field side, already visible on the individual coil signals in the form of a reduction of the 8 integrated $\tilde{b}_\theta$ signals. For the numerical integration yielding $\tilde{b}_\theta$, it was necessary to use a numerical high-pass filter (time constant ≈ 3ms) to get rid of integration drifts. A slight distortion of slow events is then introduced by this filtering. For instance, the contribution of occasional slow Mirnov oscillations is reduced and thus enhances the gong dynamic resolution. It

also explains the apparent slow decrease of the n=0 component following the sawtooth crash (see for example Fig. 5), which remains therefore essentially artificial. It is remarkable that the n=0 Shafranov shift occurs on the same time scale as the n≥1 sawtooth instability. This indicates that the $\beta_p+\frac{1}{2}l_i$ equilibrium change already starts from the beginning of the instability growth, that is before the temperature collapse itself.

The poloidal analysis is intrinsically more difficult to perform because of the geometrical deformation of the poloidal coordinate system due to toroidicity. Then, the toroidicity and the shape of the flux surfaces produce a distortion of the modes from pure Fourier components [29] and a coupling between modes of different rational surfaces [30]. As a result, only an overall behaviour like the dominant m number at the edge can be measured by a poloidal array of probes.

Figure 7 is an example of the type of poloidal analysis performed for the gong. The poloidal mode number is deduced from the poloidal plots (number of poloidal oscillations) and is roughly $m \approx 2 = \text{int}(q_\psi(a))$ with $q_\psi(a) = 2.6$ (Fig.7a). In addition, the two poloidal arrays, 180^o toroidally apart, show nicely the n=1 dominant character. For an increased $q_\psi(a)$ at the edge, like $q_\psi(a) = 4.2$ in Fig. 7b) , the corresponding m-value also increases to about 4. These m-values are expected as a result of the coupling between the different resonant surfaces. In general, the dominant m-number obtained by this means is of the order of q_ψ at the edge ($m \approx \text{int}(q_\psi(a))$ as in Fig. 7a) , though lower values ($1<m<\text{int}(q_\psi(a))$) can also transiently be observed. This fact may be attributed to the details of the radial structure of the instability: in some cases modes resonant on an intermediate integer q surface may be stronger than the one at the edge, as far as their relative amplitudes at the probe location are concerned. Note that the observation $m \approx \text{int}(q_\psi(a))$ is typical of the ballooning effect (also described as mode ballooning), likely to occur at small aspect ratio [31,32].

The gong shows some ballooning character in the form of an in-out asymmetry for limiter discharges easily visible in the examples of Fig. 7, that is for discharges leaning on the LFS limiters. For these discharges, the gong appears to be stronger at the low field side (LFS) equator. This still holds when the discharge is leaning on the inner wall and therefore with a shorter plasma coil separation on the high field side (HFS) coils than on the LFS coils. Similar in-out asymmetry has been observed for continuous m=2 Mirnov activity in JET [33].

The gong helicity sign, another characteristic quantity to trace back to the nature of the instability involved, can be deduced from the signals of two perpendicular arrays of magnetic probes. The measurements show that the gong helicity is the same sign as that of the equilibrium magnetic field. This can equivalently be deduced from the vector sum of the poloidal and toroidal phase velocities.

The toroidal rotation of the instability can be measured using the results of the toroidal Fourier decomposition. The dominant component being n=1, its phase $\phi_{n=1}(t) = \text{arc tg}\,(s_{n=1}(t) / c_{n=1}(t))$ can thus be considered as the phase of the instability itself. In Fig. 8, a plot of two consecutive gongs of the same discharge is shown. The first indicates a nearly stationary toroidal perturbation whereas the second travels with a large phase velocity of the order of $1\text{–}5\cdot10^4$ m/s in the electron drift direction during the instability growth. The difference shown by these two examples appears very typical when comparing several gongs. This also is similarly observed on the poloidal rotation as measured by the pick-up coils or by the soft X-ray cameras (see Chap.III). This erratic behaviour indicates that the instability has no preferential direction and that details of the instability time evolution are not reproducible for two successive gongs. Thus, these

rotation differences should be explained by fine details in the profiles that change from one sawtooth to the next.

III PLASMA DISPLACEMENT

As seen in the last section, the gong perturbation is detected at the same time as the sawtooth instability observed on the soft X-ray raw signals. This synchronisation indicates that the two perturbations are linked together in some way, or may represent two different observations of the same process. To show the evidence that the gong represents a direct measurement of the sawtooth instability, a parameter was found which could be measured independently by the soft X-rays and the magnetic pick-up coils. This parameter was the radial plasma displacement associated with the sawtooth instability. In this section, the edge displacement deduced from the magnetic gong signal is compared with the core motion measured from soft X-ray tomography.

The magnetic perturbation measured at the edge can be related to an edge motion, as in ideal MHD a magnetic perturbation is linked to a displacement by :

$$\vec{\tilde{b}} = \vec{\nabla} \wedge (\vec{\xi} \wedge \vec{B_o}) \qquad (3.1)$$

Evidence of an edge pertubation during the sawtooth crash can also be found in Langmuir probe measurements (Fig. 9) where the ion saturation current exhibits a signal similar to the magnetic signal at the time of the internal disruption. An estimate of the radial edge displacement $\xi_r(a)$ can be calculated using the pick-up coil measurement of $\tilde{b_\theta}$. In the cylindrical approximation with a perfectly conducting plasma of radius a and a conductive wall of radius d, where the probes are also located, the radial displacement in front of the probe becomes

$$\xi_r(a) = \frac{\tilde{b}_\theta(d)}{B_{\theta_0}(a)} \cdot \frac{d}{2m(1-\frac{nq}{m})} \cdot \left[\left(\frac{d}{a}\right)^m - \left(\frac{a}{d}\right)^m\right] \qquad (3.2)$$

where $B_{\theta 0}(a)$ is the equilibrium poloidal field.

This expression shows that the radial displacement ξ_r is directly proportional to the perturbed $\tilde{b}_\theta$ measured at the edge by a pick-up coil. With the help of the full set of toroidally distributed coils, the displacement can be decomposed in its toroidal Fourier components. Thus, the n'th mode displacement amplitude $\xi_{r_n}(a)$ is:

$$\frac{\xi_{r_n}(a)}{d} = G_{mn} \cdot \frac{b_{\theta n}}{B_{\theta_0}(a)} \qquad (3.3)$$

where $G_{mn} = \frac{1}{2m(1-\frac{nq}{m})} \cdot \left[\left(\frac{d}{a}\right)^m - \left(\frac{a}{d}\right)^m\right] \cong 0.1$ is a geometrical factor

$b_{\theta n}$ = the n^{th} Fourier component of the magnetic perturbation.

As it results from Fourier analysis , the n'th mode displacement amplitude $\xi_{r_n}(a)$ is now a non-local quantity that presents the advantage of being invariant under toroidal plasma rotation. It remains, therefore, unaffected by the various possible plasma rotation velocities observed.

This edge displacement measured from the magnetic field perturbation can be compared to the core displacement measured by the soft X-ray diagnostic. In JET, two soft X-ray cameras, viewing the plasma from the top and from the low-field-side midplane [34] allow the original soft X-ray emission profile to be tomographically reconstructed. The soft X-ray signal response is limited at high frequency by a 33 KHz 3dB cut-off. The m=1 radial plasma shift $\xi^{sx}_{m=1}$ in the centre can be obtained by calculating the first moment of the soft X-ray emission, also called the

centroid position [35]. The coordinates of the centroid are defined as follows

$$Z = \frac{\int z.f(x,z).dx.dz}{\int f(x,z).dx.dz} \quad \text{and} \quad X = \frac{\int x.f(x,z).dx.dz}{\int f(x,z).dx.dz} \qquad (3.4)$$

where f(x,z) is the tomographically reconstructed soft X-ray emissivity; the integration can either be performed over the full profile or only over the region inside the sawtooth inversion radius. The centroid displacement is then

$$\xi^{sx}_{m=1} = \sqrt{(X-X')^2 + (Z-Z')^2} \qquad (3.5)$$

the primed symbols referring to the position of the centroid before the instability growth.

In section II, the main component of the gong (magnetic) pulse was shown to be n=1. We therefore compare the amplitude of the n=1 gong mode with the m=1 centroid shift. An example of such a comparison is presented in Fig. 10 where the two displacements (Fig. 10a) are plotted on a logarithmic scale (Fig. 10b) to allow for an unknown multiplicative factor. Both displacements exhibit the same temporal behaviour and the two traces overlap almost exactly. The agreement is remarkable over the whole growth phase and for as long as the value of $b_{\theta n=1}$ is large. This already demonstrates that the gong is directly linked with the internal disruption instability. At maximum amplitude the magnetic signal is typically one order of magnitude larger than the background noise (i.e. typ. signal-to-noise ratio ≥ 10). A similar signal-to-noise ratio is obtained for the centroid measurement during ohmic sawteeth in quiescent discharges. The level of detectability is typically $0.5\text{-}1 \cdot 10^{-4}$ T for the gong measurement, corresponding to $b_{\theta n=1} / B_\theta(a) \approx 10^{-4}$. The level of detectability is typically of 1mm for the centroid motion, that is $\xi^{sx}_{m=1} / r_{inv} \approx 1\text{mm}/0.5\text{m} \approx 2\ 10^{-3}$.

We now describe the different phases of the growth, saturation and decay of the internal disruption instability. The different phases are outlined in Fig. 10b) by the vertical dashed lines.

The fast rise of the instability is observed to start some 250 μs before the central soft X-ray emission has collapsed (Fig. 10a). The fast growth itself lasts about 100 μs until saturation of the motion occurs. During this period a growth rate of $\gamma = 1.6 \cdot 10^4 s^{-1}$ is measured on the magnetic and soft X-ray diagnostics. Preceding this fast growth, it is often possible to observe a more extended phase of slow growth [35] measurable on the magnetic and soft X-ray diagnostics, provided the level of background mode activity is small (0.5×10^{-4} T and 1mm respectively). The presence of this first slow growth rate, smaller by more than one order of magnitude ($\gamma \cong 1.1 \cdot 10^3 s^{-1}$) on both diagnostics suggests two distinct growth phases. The first period of slow growth can last typically one millisecond, whereas the second period of fast growth typically lasts 50-200 μs. In the following and unless otherwise specified, growth rate analysis will always only concern this second fast growth. It must be noted that the sawtooth thermal collapse has hardly begun during the second rapid growth period.

The crash itself is only completed during the following saturation period, lasting typically 100 μs. After this saturation, both motions decay and diverge from each other. This late discrepancy between the two displacements is not surprising and only appears when the $b_{\theta n=0}$ motion is taking over from the $b_{\theta n=1}$ motion. The presence of this n=0 Shafranov shift is indeed sufficient to explain the discrepancy observed between $b_{\theta n=1}$ and $\xi^{sx}_{m=1}$ following the sawtooth collapse. While the $b_{\theta n=1}$ signal monitors a non-local toroidal mode component, the centroid motion $\xi^{sx}_{m=1}$ on the other hand gives the total m=1 displacement in one specific poloidal plane. In fact, all the n-components contribute to $\xi^{sx}_{m=1}$ (and not only the n=1 component), including the n=0 Shafranov shift which develops to a large amplitude in the late phase.

Thus, the two displacements have been demonstrated to be well correlated during the growth and saturation of the instability. An interesting corollary of this good agreement is the implicit demonstration that the soft X-rays represent an adequate monitor of the magnetic flux surfaces, at least during the growth of the instability.

The values of central and edge displacements are now compared. One should notice that the absolute value of the soft X-ray displacement depends on the extension of the integration domain used to calculate the centroid position. When the domain is restricted from the full profile (as in Fig. 10b) to the region within the inversion radius of the sawtooth (Fig. 10c), the calculated centroid displacement is typically increased from 3-4cm to 15cm, that is to about 1/3 of the inversion radius itself. The central motion is then better quantitatively represented when using the domain restriction, as noticed in [12]. In Fig. 10c) the motion of the maximum of the soft X-ray emission profile is also shown, which is moving close to the sawtooth inversion radius during the saturation phase.

The plasma edge displacement value can be calculated from $b_{\theta n=1}$ by using relation (3.2) for the example in Fig. 10. The conditions are I_p=2.2MA, $B_{\theta_o}(a)$=0.27T, $T_e(0)$=7.1KeV, $\Delta T_e(0)$=2.8KeV, B_φ=2.1T, $q_\psi(a)$=4.75, $m=int(q_\psi(a))=4$. The magnetic signals for the toroidal mode analysis have been recorded with the coil nb. 3 (see Fig. 1 for the spatial configuration) with a≅1.4m and b≅1.64m. The maximum amplitude $b_{\theta n=1} \cong 1.5 \cdot 10^{-3}$T then corresponds to the radial displacement

$$\xi_{r_{n=1}}(a) = 7 \cdot 10^{-4}\text{m}.$$

The corresponding centroid shift value is

$$\xi^{sx}_{m=1} = 0.15\,\text{m}.$$

The ratio of edge n=1 displacement to core displacement yields therefore in

this case : $\xi_{r_{n=1}}(a) / \xi^{sx}_{m=1} \approx 5 \cdot 10^{-3}$

with $q_\psi(a)$ =4.75 and b/a=1.54. Such a small ratio emphasizes that the internal disruption instability, though well observable at the edge, remains essentially an internal mode.

In this particular example, (Fig. 10) one can notice that the time evolution of the toroidal phase is not perturbed by the growth of the instability. This is not the case in most of the other examples where it is possible to observe a sharp change at the beginning of the gong. This then depends on the presence (or absence) of background Mirnov oscillations before the internal disruption. As already mentioned above (see Fig. 8) the toroidal rotation of the instability exhibits a rather erratic behaviour from sawtooth to sawtooth. However, the measurement of the poloidal rotation direction given by the centroid motion (Fig. 10c) and of the toroidal rotation given by the gong toroidal phase (Fig. 10a) can both be used together to yield the mode helicity in an alternate way. This provides the same mode helicity as already obtained from the plasma edge only with the gong.

IV THE n-SPECTRUM OF NORMAL AND MONSTER SAWTEETH

Toroidal spectra of NST have already been shown in chapter II. In the present chapter the analysis of NST will be deepened and will develop in a comparative study of NST and MST spectra. As was found in chapter III, the identity of the n = 1 gong component and of the m = 1 centroid shift deduced from soft X-rays suggests that the toroidal mode analysis performed at the edge could well yield the full poloidal spectrum of modes on the q = 1 surface. This hypothesis is made as m/n = q on rational surfaces, and therefore m = n on the q = 1 surface; we make use of the fact that a toroidal mode number n is invariant in a torus (which will be developed shortly).

developed shortly).

The measured toroidal component amplitudes decrease as a function of n and the toroidal spectrum can be approximated by $b_{\theta n}=b_{\theta n=1}\cdot n^{-\alpha}$ (for n = 1, 2, 3) where α is the spectrum index. During the growth phase of the NST, this typically yields

$$1.5 < \alpha < 3$$

as can be deduced for example from Fig. 6. In other words, the amplitude of the different modes decreases by factors of 3 to 8 for each increasing n.

In the case of MST the spectrum turns out to be quite different. A MST is shown here as an example, Fig. 11. This MST has been obtained with an additional power of P ≈ 11MW of mixed RF (central resonance, D/H-minority) and NB heating (co-injection, injection angle ~17^0). In this case the sawtooth durations τ_S has been extended from typically 0.1-0.2s to 1.47s, thus maintaining stationary T_e profiles over several confinement times. The evolution of the spectra during the growth phase at the end of a MST is quite different from that of the NST case.The n = 1 mode dominates the motion: the n = 1 component is always more than an order of magnitude higher than the n = 2 component. The ratio $b_{\theta n=2}/b_{\theta n=1}$ for MST is in the few percent range. This result can be compared with NST (Fig. 6) where the $b_{\theta n=2}/b_{\theta n=1}$ ratio is much larger (typically 20-30%). The comparison between NST and MST spectra before saturation is well summarized by Fig. 12 where the ratio $b_{\theta n=2}/b_{\theta n=1}$ is shown as a function of the sawtooth period duration.

It is also interesting to notice that the MST n=1 mode grows faster than exponentially. The respective growth rate of the n=1, 2 and n=3 component can be different (Fig. 11) and show roughly $\gamma_3 \approx \gamma_2 > \gamma_1$. This trend is not clearly marked for NST where the different modes can grow simultaneously (Fig. 6).

At full saturation of the instability, the time of n≥2 component maxima show for both NST and MST an increasing delay for increasing n, measured relative to the time of the n=1 maximum. For MST these delays are typically 30μs and 50μs for the n=2 and n=3 component respectively. These delays were shorter by a factor 3 for NST, yielding 10μs and 15μs respectively. The remaining high level of modes after the temperature crash for MST (Fig. 11) is representative of the high level of mode activity usual after MST crashes.

Comparison of the n=1,2 and 3 toroidal phase velocities also gives information about the relation between the different n Fourier components. For both NST and MST, the n=1 toroidal phase sets in typically 1.5ms before the crash. This represents the earliest sign of the instability detected by the magnetic coils; higher n phases come out somewhat later, due to a lower signal to noise ratio. In the case of NST (Fig. 13), the toroidal rotation frequency (i.e. toroidal phase time derivative $\dot{\phi} = \frac{d\phi}{dt}$) increases linearly (within ±30% error) with n:

$$(\dot{\phi}_{n=1}, \dot{\phi}_{n=2}, \dot{\phi}_{n=3}) = (1,2,3)\,\dot{\phi}_{n=1} \qquad \text{i.e.} \qquad \dot{\phi}_n = n \cdot \dot{\phi}_{n=1}$$

indicating that their phase velocities are similar:

$$v_n = \frac{\omega_n}{k_n} = \dot{\phi}_n \cdot \frac{R}{n} = \dot{\phi}_{n=1} \cdot R$$

Thus, the different n modes can be essentially viewed as the Fourier decomposition components of the same perturbation. When the n modes grow in parallel, similar phase velocities mean that the perturbation keeps its basic shape unchanged while rotating. It simply expands in size. When the n component growths are different, then shape modification occurs. However, since the phase relation between the different n still holds, this must be simply interpreted as a shape change of the perturbation and must be differentiated from the simultaneous or delayed growth of independent n

modes. For MST the same phase analysis is more difficult to perform since the n=2 and n=3 modes emerge quite late above the noise level. When measurable, no simple relation between the different component phase velocities can be found. For instance, the n=3 component rotates in the opposite direction in Fig. 11. This difference suggests that the n=1 instability may be accompanied by secondary independent n=2 or n=3 modes for MST conditions

After the crash, locking of the n = 1, 2 and 3 modes to the tokamak vessel can occur for MST, as already noticed for the n = 1 locked-mode [36]. In this example (Fig. 11) the mode locking occurs less than 100μs after the crash. This time is much shorter than the penetration time of 4ms of the vessel to a transverse field [28]. Curiously enough, all the modes don't always lock together, as for example is the case for the n=3 component of Fig. 11 which continues to turn freely for 1.1ms before locking. For large MST, the n=1 mode locking can last till the end of the discharge with negative effects on the confinement properties [36].

An important point regarding these measurements concerns the validity of the edge measured n-spectra for the representation of the n-spectrum , and possibly the poloidal m-spectrum on the q=1 surface. On the q=1 surface the n spectrum of the resonant modes is nearly equal to the m spectrum since we have m=n on this surface. Therefore, we would like to know the radial response or transfer function of a plasma to a given n-perturbation produced in the q=1 region. Various features can account for distortion of the n-spectrum: among which are a) non-axisymmetry, b) non-linearity in the radial transfer function, and c) multipolar field decay.

a) As far as non-axisymmetry is concerned, only gongs with vanishingly small preceding Mirnov oscillations have been retained in the

present analysis, as Mirnov oscillations directly perturb the measurement. As a consequence the most axisymmetric cases have deliberately been selected for this analysis.

b) We discuss here the non-linearity in the radial transfer function between the q=1 surface and the edge, though non-linearity is certainly most important in the q=1 region, where it may already couple n's [37]. If non-linearity were important for the radial transfer function, an increased spread out of the n-spectrum would be expected for MST. On the contrary a concentration on the n=1 component is experimentally observed for the large amplitude MST gongs. In addition, the comparison of NST and MST spectra both taken at the same amplitude value $b_{\theta n=1} \approx 5\ 10^{-4}T$ still shows this major difference in the two sawteeth types spectra: this is carried out by comparing a NST spectrum just before its saturation with a MST spectrum at an early stage of its growth. Furthermore, the comparison between the centroid motion and $b_{\theta n=1}$ (see chap. III) shows excellent agreement during the whole growth of the instability, that is irrespective of the mode amplitude. Thus the source of the higher n's should mainly be in the center.

c) Multipolar field decay attenuates the amplitude of higher n-modes and therefore artificially increases the spectrum indices. This decay should affect NST and MST similarly. It would mainly obliterate the spectrum shape, but not the individual component evolution nor the evolution of one component with respect to another one (relative time evolution).

The distortion introduced by these three effects should be numerically estimated for a realistic equilibrium and geometry, though such a study is outside the scope of this work. Nevertheless experimental results indicate that the distortion should be constant during the instability growth and consequently does not affect the interpretation of our results concerning the differences in the spectrum characteristics between NST and MST. That is, the measured spectra are indicative of a broad n spectrum in the q=1 region for NST and of a sharp n=1 mode on q=1 for MST.

In summary, NST present a broader n spectrum, the different n components having similar growth rate and intercoupled phase velocities. On the contrary, MST exhibit a sharper n=1 signature, a faster than exponential growth and seemingly random phase velocity relationship. These results indicate that equilibrium conditions for the sawtooth instability are different for NST and MST. The duration of the whole saturation process, as measured by the delay separating n-component peaks, is several times longer for MST than for NST.

Translating these results in terms of the m spectrum in the q=1 region, NST can be seen as a wide m buldging perturbation which rotates during the instability growth while keeping its shape roughly unchanged (locked phase relation between n-components). On the other hand MST can be seen as a sharp n=1 rotating perturbation, and therefore probably also m=1, accompanied by higher independent n modes only just before the crash (no particular phase relation between n components).

V n=1 AMPLITUDE AND GROWTH RATE PARAMETRIC STUDY

The perfect proportionality between the gong amplitude and the centroid shift allows the gong to be used for the study of the amplitude and growth rate γ of the internal disruption instability, and to study their dependence on plasma parameters, such as plasma current I_p, safety factor $q_\psi(a)$, central electron temperature Te(0), sawtooth period τ_s, etc.

a) Amplitude and growth rate calculations

The analysis of the amplitude and growth rate is performed by taking fast sampled data (40KHz sampling frequency during 200ms). For each

gong the growth rate is calculated as follows, assuming an exponentially growing instability of the form:

$$\tilde{b}(x,t) = b_0 \mathrm{Re}\left[e^{i(\mathbf{k}\cdot\mathbf{x}-\phi_0(t))}\right] e^{\gamma t} \qquad (5.1)$$

where $\phi_0(t)$ is the phase due to the mode rotation. The amplitude of the instability is $A(t)=b_0 e^{\gamma t}$ and an estimate of the growth rate γ can be obtained:

$$\gamma = \frac{dA(t)}{dt} \cdot A(t)^{-1} \qquad (5.2)$$

The last expression is valid for any mode and therefore also for $b_{\theta\, n=1}$, the main component of the gong instability. Because of the time variation of the calculated growth rate, an averaged γ is calculated over a period of several time points around the time for which the amplitude reaches half of the peak amplitude of the n=1 mode, largely before any visible sign of saturation of the mode. It must be noticed that the time derivative of $b_{\theta\, n=1}$ is not equivalent to the n=1 component of the raw (unintegrated) data:

$$\frac{d}{dt}(b_{\theta n=1}) = \gamma \cdot b_{\theta n=1} \qquad (5.3)$$

whereas

$$\left(\frac{d}{dt} b_\theta\right)_{n=1} = (\gamma + i\frac{d}{dt}\phi(t)) \cdot b_{\theta n=1} \qquad (5.4)$$

The extra component $i\frac{d}{dt}\phi(t)$ in (5.4) is due to the rotation of the mode itself.

The possible distortion of the measured growth rate due to the limited bandwidth used in the measurements is now estimated. At the high-frequency side, as mentioned above, a 10 KHz cut-off (-3dB) originates from the inconel probe casing. At the low-frequency side, an artificial high-pass

time constant of 3 ms has been introduced in the calculation to remove numerical integration drifts due either to electronic drifts or to background lower frequency Mirnov oscillations. Simulations show that the calculated growth rates are not significantly affected by these effective high-pass and low-pass filters in the range of the observed growth rates $1.5 \cdot 10^3 < \gamma < 9 \cdot 10^4$ s^{-1}, nor is it by the 40KHz sampling rate.

However, perturbative effects on the measurement of γ arise from the presence of underlying Mirnov activity. It has therefore been necessary to select the sawteeth used in this chapter among "quiescent" sawteeth, that is without any marked precursor oscillations.

b) n = 1 mode amplitude

In the following, we first focus attention on NST, we then compare the results with the MST. The plasma current (I_p) values for the NST data base used in this chapter were 2, 2.8 and 4 MA with a constant toroidal magnetic field of 3.4 Tesla. Only ohmic shots or shots with very low ICRH power (P_{RF}<1MW) were used. The analysis shows that the amplitude of $b_{\theta n=1}$ reached at the end of the sawtooth crash, that is the value at saturation, is proportional to the amplitude of the electron temperature drop on axis $\Delta T_e/T_e$ (Fig. 14) for NST, when keeping the same main discharge parameters I_p, $q_\psi(a)$, and B_φ. A similar result is obtained when shown against $\Delta T_e(0)$. This indicates the presence of a quantitative link between the edge magnetic perturbation and the amplitude of the central temperature or pressure perturbation for the same magnetic geometry.

MST show comparatively stronger gong perturbations: in Fig. 15 are shown the values of $b_{\theta n=1}$ versus $\Delta T_e(0)/T_e(0)$ for some MST data. These values all sit above the NST extrapolation (left lower corner) by up to nearly an order of magnitude. The value of an RF heated NST, taken out of the

same MST shot series, is also shown in Fig. 15 as a reference. The parameters of the shots and the symbols used in this figure are summarised in Table I. The MST data in Fig. 15 cover wider experimental conditions (different $q_\psi(a)$, I_p, B_φ and P_{RF}) when compared to the NST data in Fig. 14 thus a larger scattering is expected (see for instance the next paragraph for the $q_\psi(a)$ effect on the $b_{\theta n=1}$ measurement).

The gong amplitude has been observed to be larger at the low $q_\psi(a)$ values and to become nearly undetectable at high $q_\psi(a)$. This trend can already be seen in Fig. 16 where NST are taken from only a narrow safety factor range: $5.0<q_\psi(a)<6.4$. The reduction in amplitude observed at high $q_\psi(a)$ can be attributed to several experimentally inseparable factors. These are, as $q_\psi(a)$ increases, (i) the reduced volume encompassed by the q=1 surface, (ii) the increased geometrical separation between the q=1 radius and the measuring coil, (iii) the increased number of resonance surfaces placed between the q=1 surface and the plasma edge, (iv) the likely larger m number of the gong for larger q, which produces a faster multipole roll-off.

The amplitude of $b_{\theta n=1}$, and therefore also the displacement $\xi^{sx}_{m=1}$ are also seen to be linked to the sawtooth duration τ_s preceding the crash. For NST, this is shown in Fig. 17 where the amplitude increases statistically with sawtooth period τ_s. In addition it can be noticed that the regression line through the points suggests that a minimum time of 50 ms (for the conditions in this series of shots) is needed to yield a non-zero signal. In other words, this is the minimum time needed after the crash to restore an equilibrium magnetic configuration which is again unstable with respect to an internal disruption. This represents a dead time for the instability after the sawtooth crash. For MST, that is for large τ_s values, the $b_{\theta n=1}$ amplitude is much larger than for the NST, as shown in Fig. 18, (shot parameters in Table I). As already noticed for the comparison between $b_{\theta n=1}$ and ΔT_e (see Fig. 17), the MST data exhibit a much larger scattering.

The previous sections have shown that $b_{\theta n=1} \sim \xi^{sx}_{m=1}$ during the time evolution of the instability growth and that $b_{\theta n=1} \sim \frac{\Delta T_e(0)}{T_e(0)}$ for NST. These relations demonstrated the central origin of the magnetic signal. These results also suggest a combined scaling:

$$b_{\theta n=1} \sim \xi^{sx}_{m=1} \cdot \frac{\Delta T_e(0)}{T_e(0)} \qquad (5.5)$$

which, by taking into account $b_{\theta n=1} \sim \tau_s$, valid only in a statistical sense (Fig. 17), presents some analogy with a relation proposed by Wesson for NST [38] :

$$\tilde{b} \sim \xi_{instability} \cdot \frac{\Delta T_e(0)}{T_e(0)} \cdot \frac{\tau_S}{\tau_R} \qquad (5.6)$$

where $\tilde{b}$ is the magnetic perturbation within the central region, τ_s is the sawtooth period and τ_R is the characteristic resistive diffusion time ($\tau_R = \frac{\mu_0}{4\eta} \cdot r_1^2$ with η the resistivity and r_1 such that $q_\psi(r_1)=1$).

c) Growth rates

Attempts to correlate the growth rate γ with some plasma parameters using the same NST data base to find a significant scaling law have basically remained unsuccessful: this is the case in Fig. 19a) showing γ versus $\Delta T_e/T_e$ and in Fig. 19b), showing γ versus the n=1 gong component $b_{\theta n=1}$. Both figures show a large dispersion. To illustrate this point, two consecutive NST gongs from the same discharge are presented in Fig. 20. The growth rate reaches $\gamma \approx 9 \cdot 10^3$ s^{-1} for the first gong and only $\gamma \approx 1.5 \cdot 10^3$ s-1 for the second one, though the macroscopic conditions are identical. The growth rate value can indeed vary by up to nearly one order

of magnitude for two consecutive NST internal disruptions while discharge parameters such as I_p, $q_\psi(a)$, n_e, $T_e(0)$, β_p remain virtually unchanged. It is therefore not surprising that no precise scaling stems out of a parametric study for the growth rate of NST. Random variations of the gong rotation have also been observed (Fig. 8).

Although the growth rates of NST show an important scatter in Fig. 19b), it is statistically increasing with the the amplitude of the $b_{\theta n=1}$ gong perturbation measured at the edge. The same trend is also noticeable for MST, Fig. 21a), where growth rates in excess of $5 \cdot 10^4$ s^{-1} have been measured. The MST growth rates remain however a factor three below the linear extrapolation of NST (left lower corner in Fig. 21a). MST would therefore seem to obey a different scaling law, which is consistent with the observed $T_e(0)$ saturation for MST. When compared to NST, a lower dispersion of the growth rates is observed when the growth rate is plotted against the sawtooth duration τ_s, Fig. 21b).

VI SUMMARY AND DISCUSSION

The analysis of the magnetic signals associated with the sawtooth instability has allowed us to characterise the different nature of the NST and MST. In this chapter we summarise the results and discuss some of their implications. Table II gives an overview of the results.

The proportionality between $\xi^{sx}_{m=1}$ and $b_{\theta\, n=1}$ (Fig. 10b) through q = m/n on the q = 1 surface has shown that the n = 1 mode wavefunction 1) is non-zero at the edge, and 2) that it reaches the edge without major deformation in time. These facts triggered a strong interest in following the higher n-components at the edge in their own right, and also as an alternative measurement of the m-components at q=1.

The NST instability spectrum is characterised by a slowly decreasing spectrum with the different n-components growing in parallel and with their phase velocities being similar ($v_{\phi\, n} \approx v_{\phi\, n=1}$). Thus, the n=1, 2 and 3 modes are not independent modes and must be viewed as the Fourier components of a single buldging perturbation, which is typical of a ballooning type perturbation. The MST instability spectrum, on the contrary, is largely dominated by the n=1 mode, which grows independently from the other components, since there is no particular phase relation between the different n-components. The MST instability shows therefore rather the character of a kink motion.

The fact that NST and MST instabilities spatial deformations appear as essentially different suggests that different equilibrium conditions prevail in the two cases. The first major difference is the continuously decreasing central q(0) measured by polarimetry, as the sawtooth period increases, giving typically $q(0) = 0.8 \pm 0.15$ for NST and $q(0) = 0.7 \pm 0.1$ for MST [39,40], with larger $\Delta q(0)$ excursions at each sawtooth crash [10]. Second, the pressure and temperature profiles are more peaked for MST, with high saturated central values ($T_e(0)$ = 5-9 keV, β_p = 0.35-0.50, for the examples of the figures), whereas for NST these values are still rising and sizeably lower (T_{eo} = 3-4keV, β_p = 0.10-0.15). The longer delay for MST between the component maxima at saturation, several times longer than for the NST, could originate from the larger amount of flux to be rearranged in a MST instability crash, as polarimetry confirms [10]. For what concerns the difference in spectra, resistive self-consistent equilibrium simulations show that large $\Delta q(0)$ excursions at the sawtooth crash correspond to narrower spectra, more concentrated on the n=1 mode [41]. Therefore the trend of the gong-spectra observed, taking into account the $\Delta q(0)$ excursions measured for NST and MST, fits well in this frame.

A discussion concerning the possible deformation brought to the n-spectrum as it couples to the plasma edge has been given in Chap. IV. Basically, it has been shown that if there were distortions, these do not

question the difference between NST and MST n-spectra. Interactions between different m-components on the q = 1 surface may however occur. Toroidal and resistive effects can indeed superimpose higher (m,1) contributions to the basic (m,n) = (1,1) component on q = 1 [14], however remaining at low level. This shows that the dominant mode on q = 1 is m = n = 1. This suggests that NST have a spread poloidal m-spectrum on the q = 1 surface whereas MST exhibit an almost pure m = 1 mode. To be strictly correct however, we will continue to speak about n-spectra rather than m-spectra on the q = 1 surface.

The instability growth rate for both NST and MST is not constant and is in fact generally a continuously increasing function of time, as can be seen from the $b_{\theta n=1}$ traces in the many figures presented. In many of the observed cases, it is possible to separate the growth into two distinct phases: a fast growing instability, generally preceded by a slow growing instability, which we will call the precursor instability. This slow instability can as well be measured at the edge ($b_{\theta n=1}$) as in the core ($\xi^{sx}_{m=1}$), and is shown in the Fig. 10b) for NST and in Fig. 11 for MST. It was not possible to perform a spectrum analysis of this first slow precursor instability, since the signal to noise ratio, at this early time of the sawtooth, only allows the n=1 component to be measured faithfully. The precursor growth rate is typically one order of magnitude smaller than the main growth rate (see summary Table II). As a consequence, this paper only describes this main growth rate. As a whole, the sawtooth instability grows faster than exponential, which means that the instability consists of a succession of different instabilities. This can be seen from the displacement, where a two-step instability is often measured. It can also mean that the equilibrium quantities are changing during the instability growth.

To look at the issue of equilibrium changes during the growth phase, let us use the information contained in the n = 0 gong component, which is

the consequence of a $\beta_p + l_i/2$ decrease, and seen as a decrease of all b_θ traces measured with LFS coils (Fig. 5). The n = 0 traces (see for example in Fig. 5, 11, and 20), show that the equilibrium already begins to change during the growth of the instability. The maximum equilibrium rate of change occurs close to the n = 1 component maximum, which is also the position of maximum excursion of the soft X-ray centroid. Once the n = 1,2,3, ... components have saturated, the equilibrium freezes again. The fast equilibrium change that the plasma undergoes during the growth of the instability is an excellent candidate for explaining the non-constant growth rate measured. Therefore both equilibrium and growth evolution rates indicate non-linear phenomena.

The two main sequences in the instability growth rate (for both NST and MST) have suggested considering schemes with a sequence of instabilities, for instance two-step instabilities where a first instability, by modifying the equilibrium, induces a second instability, such as proposed by Bussac [42-44]. In such scenarios, an island can drive an ideal kink unstable [42,43], which in turn can drive ballooning modes unstable [44], or a resistive m=n=1 kink develops slowly into a saturated state which suddenly releases the energy in a fast growing kink [45]. Simulations with resistive, self-consistent equilibrium evolution reproduce well many features of the sawtooth activity in small and medium size tokamaks [41], but cannot yet be used to compute sawtooth activity in large tokamaks, due to the Lundquist numbers beeing too large.

The growth rate is also noticed to change by almost one order of magnitude for identical global conditions, such as in the case of two successive NST. The growth rate must therefore depend on local profile values, such as q(r) or $\beta_p(r)$, for instance. Pellet ablation measurements in NST [46] indicate a rather low shear of q(r) around the q=1 surface. Small changes in $\nabla q(r)$ at the q=1 surface in Textor [9] are shown to influence the stability of the m=1.

Although the statistics for MST is limited, it seems that MST show a more predictable growth rate (Fig. 21a) compared to NST (Fig. 19b). This may originate from steeper gradients $\nabla q(r)$ at the q=1 surface, or possibly from the simpler nature of the MST instability, made practically of only one independent n=1 kink mode.

It was noticed that two successive sawteeth can have very different growth rates. This growth rate does not seem to influence the spectrum shape in the example of Fig. 20, appart from a multiplicative factor $\Delta T_e/T_e$, which affects all the components.

VII CONCLUSION

The sawtooth instability, that is the instability terminating the sawtooth oscillation, has been studied by measuring its wavefunction using edge magnetic probes. This paper presents the first measurements using this method.

The knowledge of the n- or m-spectrum on the q=1 surface is of importance for the understanding of the sawtooth instability in tokamaks. Soft X-ray cameras measurements imply the use of tomographic reconstructions for which the capability to resolve high m's depends on the number of camera used and requires a large number of signals to be treated. The use of an array of only eight magnetic b_θ–probes can yield the n=0,1,2,3 toroidal spectrum components and has prooved to be powerful in revealing the detailed time evolution of these n-components, and by association the m-components on q=1. One major attractive advantage of the magnetic data processing is that it only involves simple FFT calculations and requires no model assumption.

The similarity in time of the n=1 magnetic perturbation with the m=1 displacement of the flux surfaces in the core demonstrates the potential of edge magnetic measurements to determine the wavefunction of the

instability on the q=1 surface. The different nature of NST and MST has been firmly established. From the geometry of the perturbation, NST exhibit a ballooning-like character, while MST show rather the character of an n=1 kink-motion. The results show that non-linearity has to be invoked both in order to describe the faster than exponential growth and because equilibrium changes occur during the growth of the instability.

Acknowledgements

We would like to acknowledge B. de Kock and G. Tonetti for making the magnetic diagnostics available. We would also like to acknowledge discussions with M.N. Bussac, R. Granetz, F. Troyon and A. Turnbull. It is a pleasure to recall here the many stimulating discussions with A. Bondeson and we are endebted for his helpful comments on the manuscript. We also acknowledge the support of P.E. Stott and F. Troyon. We would like to thank the JET staff, in particular the RF-Heating team, the ECE and Plasma Boundary Group for experimental support. This work was undertaken under Task Agreement between CRPP and JET (CRPP TA/1) and has been partly supported by the Fonds National Suisse de la Recherche Scientifique.

REFERENCES

[1] VON GOELER, S., STODIEK, W., SAUTHOFF, N., Phys. Rev. Lett. 33 (1974) 1201.

[2] CAMPBELL, D.J., START, D.F.H., WESSON J.A. et al., Phys. Rev. Lett. 60 (1988) 2148.

[3] WHITE, R.B., RUTHERFORD, P.H., COLESTOCK, P. and BUSSAC, M.N., Phys. Rev. Lett. 60 (1988) 2038.

[4] COPPI, B., HASTIE, R.J., MIGLIULIO, S., PEGORARO, F., PORCELLI, F., Phys. Lett., 132A (1988) 267.

[5] ROSENBLUTH, N.M., DAGAZIAN, R.Y., RUTHERFORD, P.H., Phys. Fluids 16 (1973) 1894.

[6] KADOMTSEV, B.B., Fiz. Plazmy 1 (1975) 710; Sov. J. Plasma Phys. 1 (1975) 389.

[7] EQUIPE TFR, 6th Int. Conf. on Plasma Phys. and Contr. Nucl. Fus. Res., IAEA, Berchtesgaden 1976, Vol. I, (1977) 279.

[8] DUBOIS, M.A., MARTY, D.A., POCHELON, A., Nucl. Fus. 20 (1980) 1355.

[9] SOLTWISCH, H., STODIEK, W., MANICKAM. J., SCHLUTER, J., 11th Int. Conf. on Plasma Phys. and Contr. Nucl. Fus. Res., IAEA, Kyoto 1986, Vol. I, (1987) 263.

[10] O'ROURKE, J., Plasma Phys. Contr. Fusion 33 (1991) 289.

[11] DE CHAMBRIER, A., DUPERREX, P.A., HEYM, A., HOFMANN, F., JOYE, B., KELLER, R., LIETTI, A., LISTER, J.B., POCHELON, A., SIMM, W., Phys. Lett. 92A (1982) 279.

[12] EDWARDS, A.W., CAMPBELL, D.J., ENGELHARDT, W.W., FAHRBACH, H.U., GILL, R.D., GRANETZ, R.S., TSUJI, S., TUBBING, B.J., WELLER, A., WESSON, J.A., ZASCHE, D., Phys. Rev. Lett 57 (1986) 210.

[13] BUSSAC, M.N., PELLAT, R., EDERY, D., SOULE, J.L., Phys. Rev. Lett. 35 (1975) 1638.

[14] BUSSAC, M.N., EDERY, D., PELLAT, R., SOULE, J.L. 6th Int. Conf. on Plasma Phys. and Contr. Nucl. Fus. Res., IAEA, Berchtesgaden 1976, Vol. I, (1977) 607.

[15] COPPI, B., GALVAO, R., PELLAT, R., ROSENBLUTH, M., RUTHERFORD, P., Fiz. Plazmy 2 (1976) 961 and Sov. J. Plasma Phys. 2 (1976) 533.

[16] WESSON, J.A., Nucl. Fus. 30 (1990) 2545.

[17] DRAKE, J.F., KLEVA, R.G., Phys. Rev. Lett. 66 (1991) 1458.

[18] DUPERREX, P.A., KELLER, R., POCHELON, A., TONETTI, G., Helvetica Physica Acta 58 (1985) 85.

[19] DUPERREX, P.A., KELLER, R., MALACARNE, M., POCHELON, A., 12th EPS Conf. on Contr. Fusion and Plasma Physics, Budapest, Edit.: EPS, Geneva.Vol. 9F, Part I (1985) 130.

[20] DUPERREX, P.A., POCHELON, A., EDWARDS, A., GRANETZ, R.S., SNIPES, J., 15th EPS Conf. on Contr. Fusion and Plasma Heating, Dubrovnik, Vol. 12B, Part I (1988) 362.

[21] ALEXANDER, K.F., HINTZE, W., LAUX, M., PECH, P., WOLFF, H., CHICHEROV, V.M., Nucl. Fus. 24 (1984) 631.

[22] KNIGHT, A.J., POCHELON, A., SIMM, W.: in the TCA tokamak, R/a = 0.615m/0.18m = 3.4, the magnetic gong signal was below the level of detection of a single magnetic probe, even in low q discharges (1986), but becomes measurable in presence of central ECRH power deposition (1990).

[23] McGUIRE, K.M. et al., 11th. Int. Conf. on Plasma Phys. and Contr. Nucl. Fusion Res., IAEA, Kyoto 1986.Vol. I, (1987) 421; McGUIRE, K.M. et al., Plasma Phys. and Contr. Nucl. Fusion, 30 (1988) 1391.

[24] STRAIT, T., Private communication (1987); and SIMONEN, T.C., et al., Phys. Rev. Lett. 61 (1988) 1720, Fig. 3d).

[25] TFR group, private communication (1978).

[26] SNIPES, J.A., GENTLE, K.W., Nucl. Fus. 26 (1986) 1507.

[27] MALACARNE, M., DUPERREX, P.A., Nucl. Fusion 27 (1987) 2113.

[28] CORE, W.G., NOLL, P., JET Report JET-R (88) 03.

[29] MEREZHKIN, V.G., Sov. J. Plasma Phys. 4 (1978) 152.

[30] BUSSAC, M.N., EDERY, D., PELLAT, R., SOULE, J.L., 6th Int. Conf. on Plasma Phys. and Contr. Nucl. Fus. Res., IAEA, Berchtesgaden 1976, Vol I (1977) 607.

[31] TROYON, F., Course and Workshop on Basic Physical Processes of Toroidal Plasmas, Varenna (1985), Commission of the European Communities and Monotypia Franchi Città di Castello (PG) Italy, Vol. I (1985) 259.

[32] TURNBULL, A.D., TROYON, F., Nucl. Fus. 29 (1989) 1887.

[33] HENDER, T.C., ROBINSON, D.C., SNIPES, J.A., Plasma Phys. and Contr. Nucl. Fusion Res., Proc. 11th Conf., Kyoto, IAEA, Nucl. Fusion, Suppl. 1987, Vol. I (1986) 291.

[34] EDWARDS A.W., FAHRBACH, H.-U., GILL, R.D., GRANETZ, R.S., OORD, E., SHRAMM, G., TSUJI S., WELLER, A., ZASCHE, D., Rev. Sci. Instrum. 57 (1986) 2142.

[35] GRANETZ, R.S., EDWARDS, A.W., GILL, R.D., WELLER, A., 14th EPS Conf. on Contr. Fusion and Plasma Physics, Madrid, Vol. 11D, Part III (1987) 1256.

[36] SNIPES, J.A., CAMPBELL, D.J., HAYNES P.S., HENDER, T.C., HUGON, M., LOMAS, P.J., LOPES CARDOZO, N.J., NAVE, M.F.F., SCHÜLLER, F.C., Nucl. Fusion 28 (1988) 1085.

[37] BONDESON, A., private communication (1991).

[38] WESSON, J.A., private communication (1987).

[39] O'ROURKE, J., BLUM, J., CORDEY, J. G., EDWARDS, A., GOTTARDI, N., KEEGAN, B., LAZZARO, E., MAGYAR, G., STEPHAN, Y., STUBBERFIELD, P., VERON, D., ZASCHE, D., 15th

EPS Conf. on Contr. Fusion and Plasma Heating, Dubrovnik, Vol. 12B, Part I (1988) 155.

[40] CAMPBELL, D.J. et al., 12th Int. Conf. on Plasma Physics and Contr. Nucl. Fusion Res., IAEA, Nice 1988, Vol. I (1989) 377.

[41] VLAD, G., BONDESON, A., Nucl.Fus. 29 (1989) 1139.

[42] BUSSAC, M.N., PELLAT, R., SOULE, J.L. and TAGGER, M., Phys. Lett. 105A (1984) 51 ; and Phys. Lett. 109A (1985) 331.

[43] BUSSAC, M.N., LEHRBINGER, K., PELLAT, R., TAGER, M., 11th. Int. Conf. on Plasma Phys. and Contr. Nucl. Fusion Res., IAEA, Kyoto 1986, Vol II (1987) 17.

[44] BUSSAC, M.N., PELLAT, R., Phys. Rev. Lett. 59 (1987) 2650.

[45] SATO, T., NAKAYAMA, Y., HAYASHI, T., WATANABE, K., HORIUCHI, R., Phys. Rev. Lett. 63 (1989) 528.

[46] PEGOURIE, B., DUBOIS, M.A., Nucl. Fus. 29 (1989) 745, and GILL, R.D., EDWARDS, A.W, WELLER, A., Nucl. Fus. 29 (1989) 821

Table I. Shot parameter for MST data (for Fig. 15, 18, 21a and b)

	13412-20	19735-62	16052, 16448
B_φ (T)	2.8	3.0	3.0, 3.1
I_p (MA)	3.0-3.3	3.0-3.2	2.9
$q_\psi(a)$	4.3-5.8	3.0-3.2	3.7
b/a	1.54	1.4	1.4
P_{RF} (MW)	~8.	5.-9.	8., 3.
ICRH-scheme	D/H (12-14)	D/H (35-52)	D/H
	He^3/H (15-20)	He^4/H (54-62)	
	(Majority/Min.)		
P_{NBI} (MW)	0.	0.-10.	4., 5.5
	■ MST	● MST	▲▼ MST
	□ heated NST	L ● LFS heated MST (3.3T)	
	∇ partial ST	H ● HFS heated MST (2.85T)	

Table II.

	NST	MST
Amplitudes:	$b_{\theta\, n=1} < 4\cdot10^{-4}$ Tesla	$3 < b_{\theta\, n=1} < 8\cdot10^{-3}$ Tesla
Growth rates:		
precursor instab.	$\gamma \sim 10^3\ s^{-1}$	$\gamma \approx 4\text{-}5\cdot10^3\ s^{-1}$
main instability	$\gamma \leq 2\cdot10^4\ s^{-1}$ τ = 50-400μs (large dispersion)	$3 \leq \gamma \leq 9\cdot10^4\ s^{-1}$ τ = 10-30μs
Spectra:		
analysed modes	n = 0,1,2,3,cos(4φ)	n = 0,1,2,3,cos(4φ)
$b_{\theta\, n=2}/b_{\theta\, n=1}$ ratio	0.15 - 0.36	0.03 - 0.06
Saturation delay between successive modes $\tau_{1\text{-}2}^{sat}$ and $\tau_{2\text{-}3}^{sat}$	$\tau_{1\text{-}2}^{sat} \sim 10$ μs $\tau_{2\text{-}3}^{sat} \sim 15$ μs	$\tau_{1\text{-}2}^{sat} \sim 30$ μs $\tau_{2\text{-}3}^{sat} \sim 50$ μs
Phase and phase velocity	$(\dot{\phi}_{n=1},\dot{\phi}_{n=2},\dot{\phi}_{n=3}) \approx (1,2,3)\cdot\dot{\phi}_{n=1}$ i.e. $v_{\phi\, n} \approx v_{\phi\, n=1}$	no characteristic phase relation observed between the n=1,2,3 modes
safety factor q(0)	0.8 ± 0.15 [40]	0.7 ± 0.1 [40]
poloidal beta: β_p	0.10 - 0.15	0.35 - 0.50
$T_e(0)$	2.8 - 3.8KeV	5 - 9KeV steep gradients inside q=1 with enlarged inversion radius, see Fig.3 in [2].

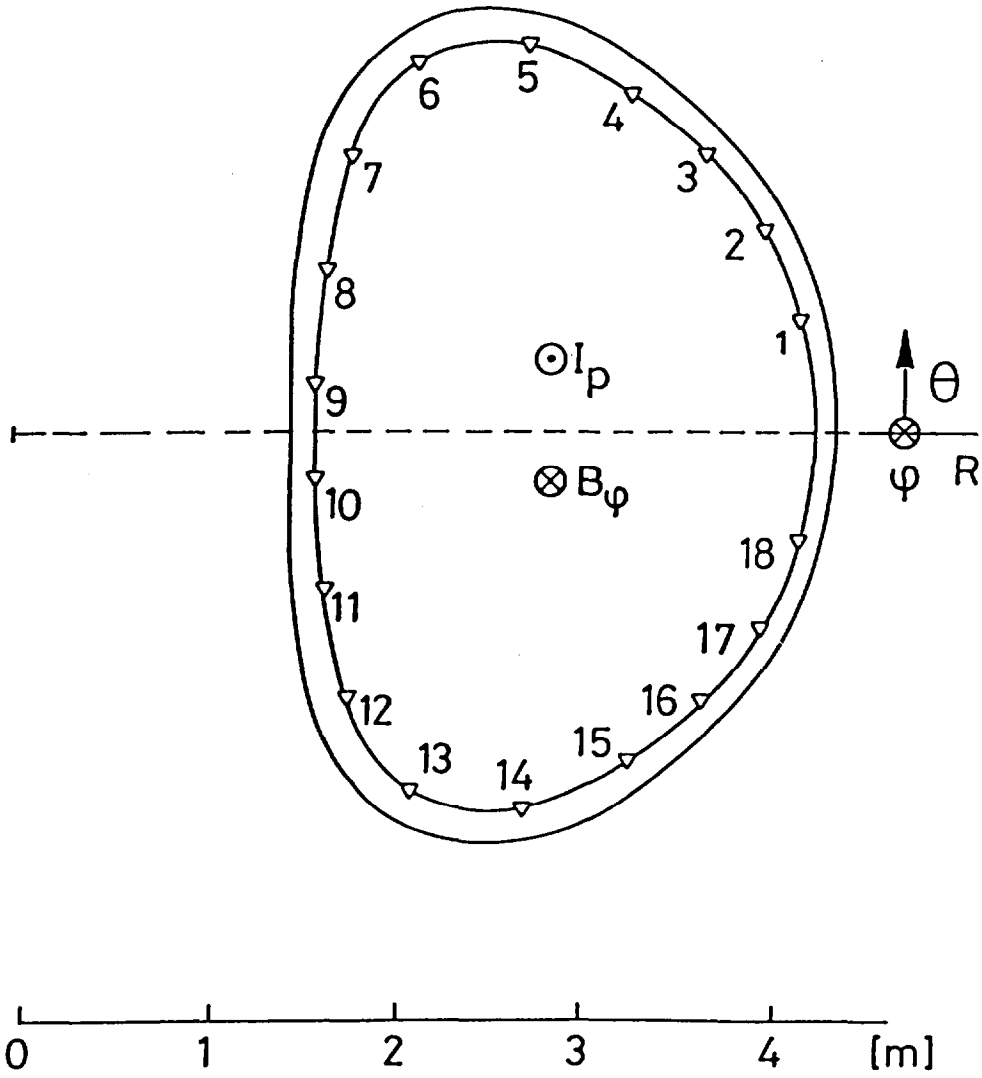

Fig. 1 : Position of the 18 magnetic coils b_θ in an octant of JET. The standard directions of plasma current and toroidal field are indicated.

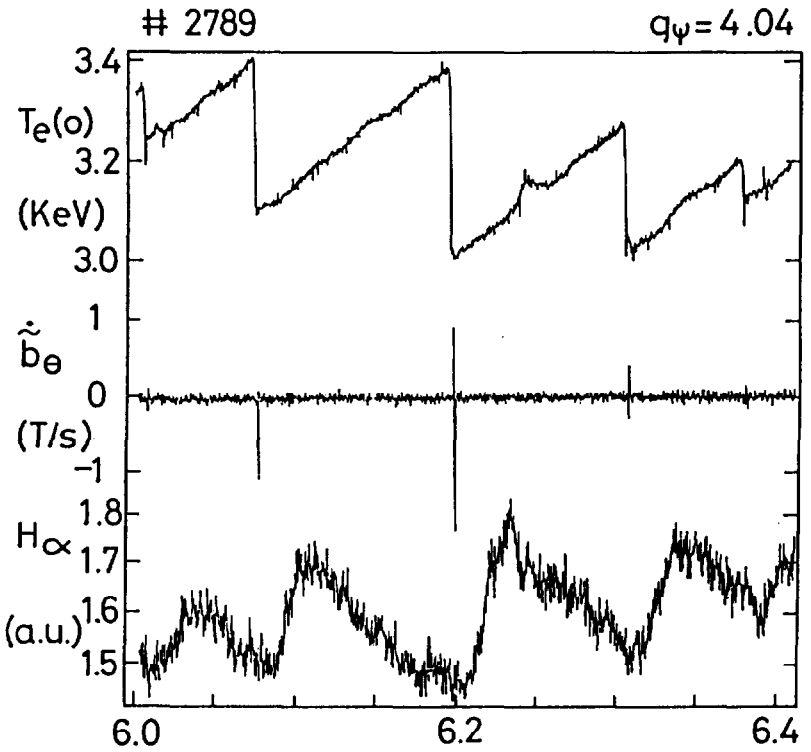

Fig. 2 : Evidence of "spikes" on the magnetic signal correlated with the central temperature collapse of the sawtooth. The maximum of the H_α signal (indicative of the heat pulse reaching the edge) occurs far later.

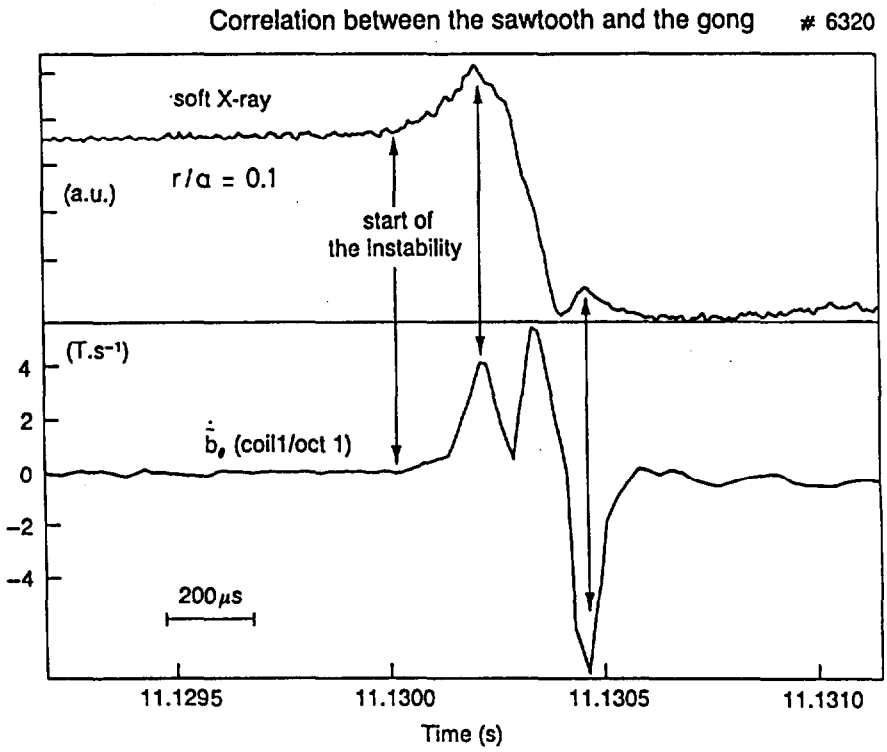

Fig. 3 : Detailed time correlation between a magnetic coil and a central soft X-ray channel. The instability start and the following transients are simultaneously visible on both signals.

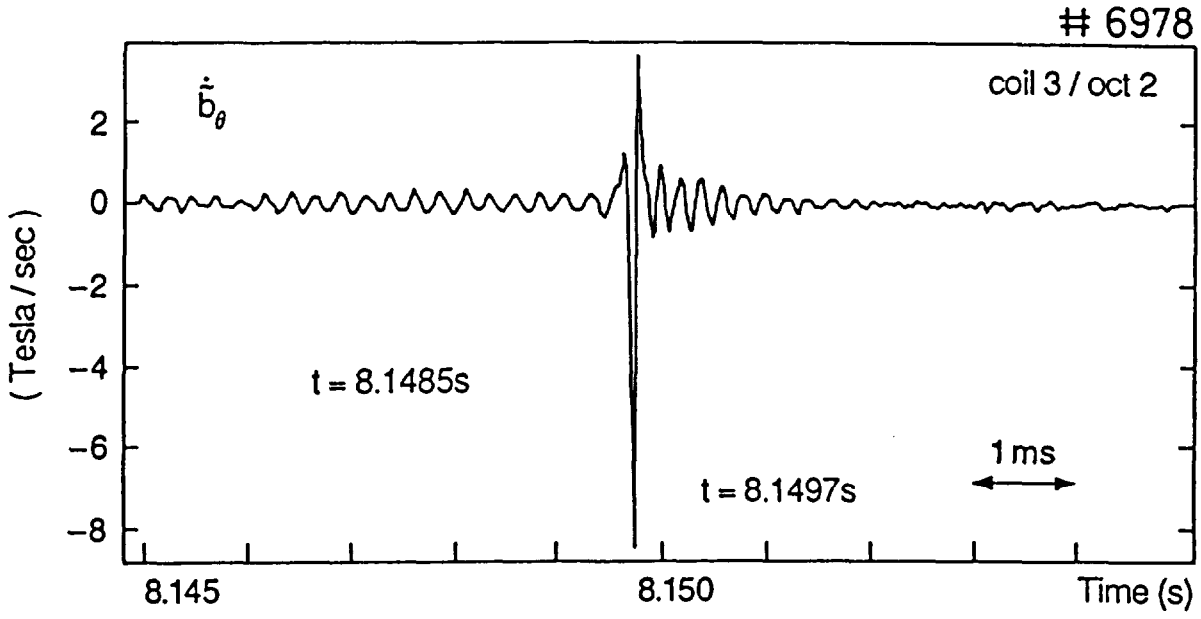

Fig. 4 : Gong occurring during an ongoing Mirnov activity.

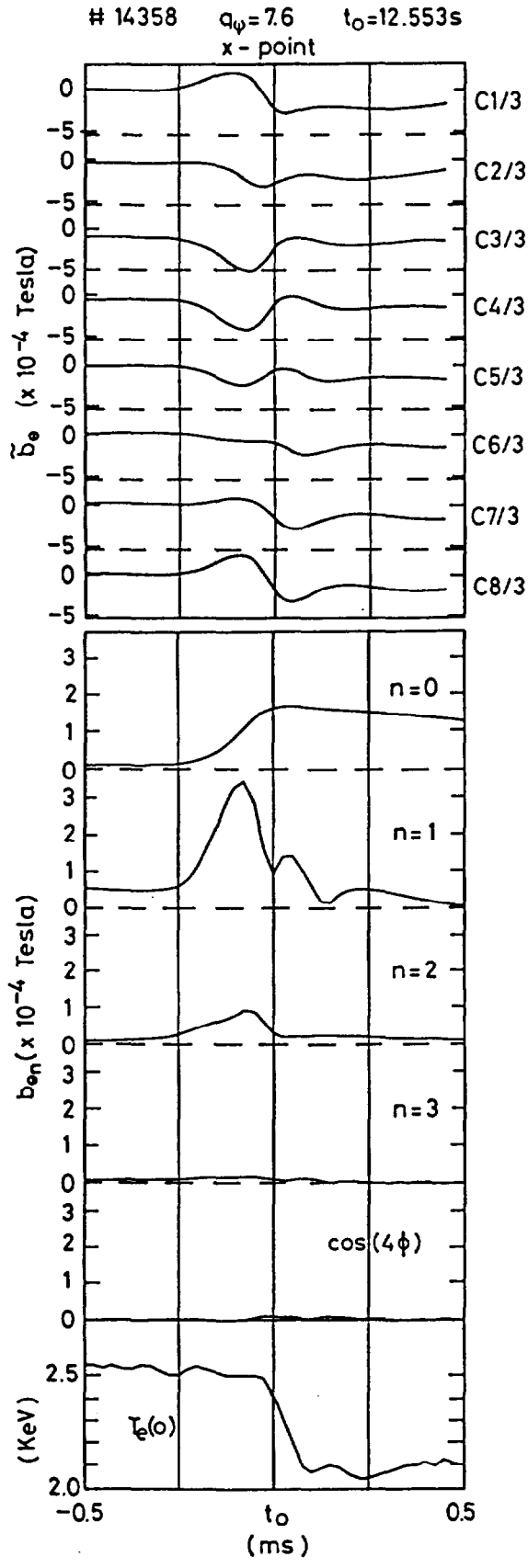

Fig. 5 : Time evolution of the 8 $\widetilde{b_\theta}$ (integrated $\tilde{b}_\theta$) and the calculated n=0, 1, 2, 3 and n=4 cosine components. The n=1 component dominates the toroidal spectrum.

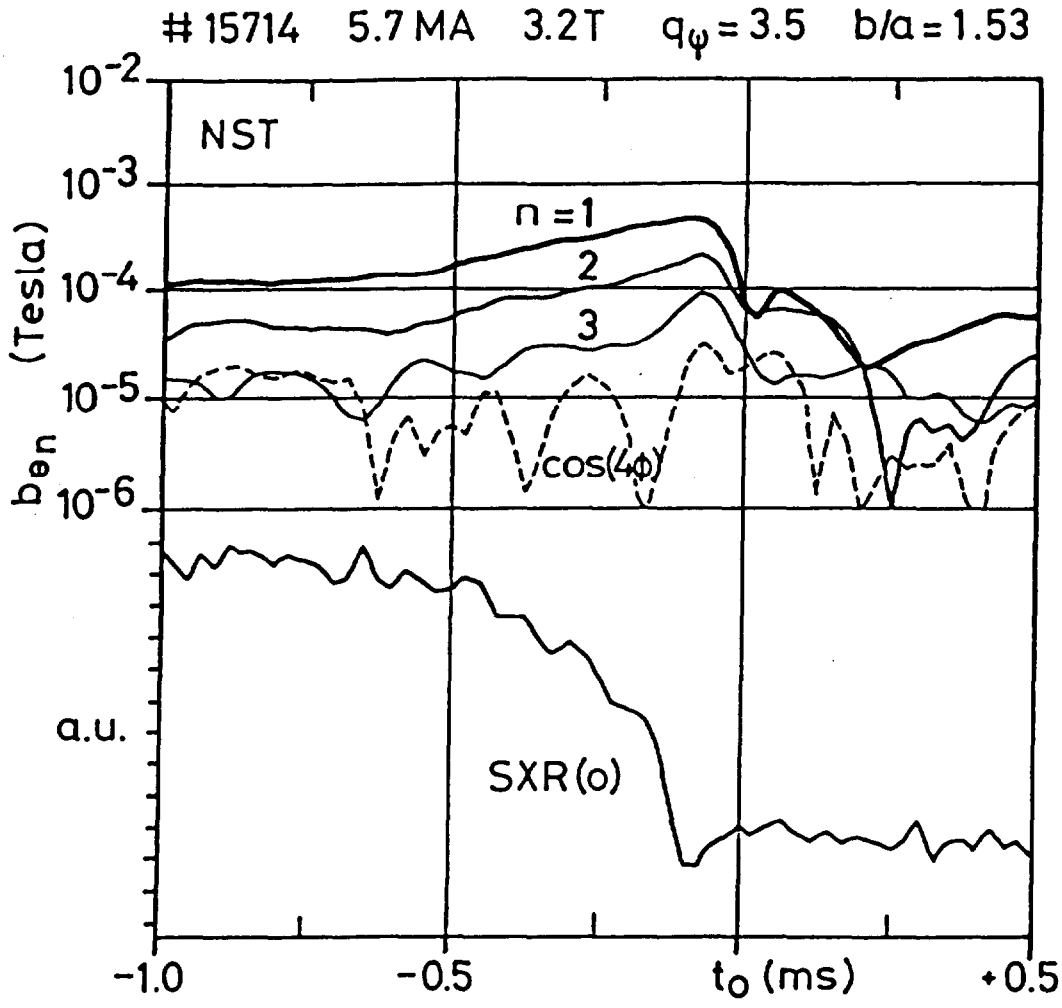

Fig. 6 : Toroidal spectrum of the gong instability for a normal sawtooth (NST).

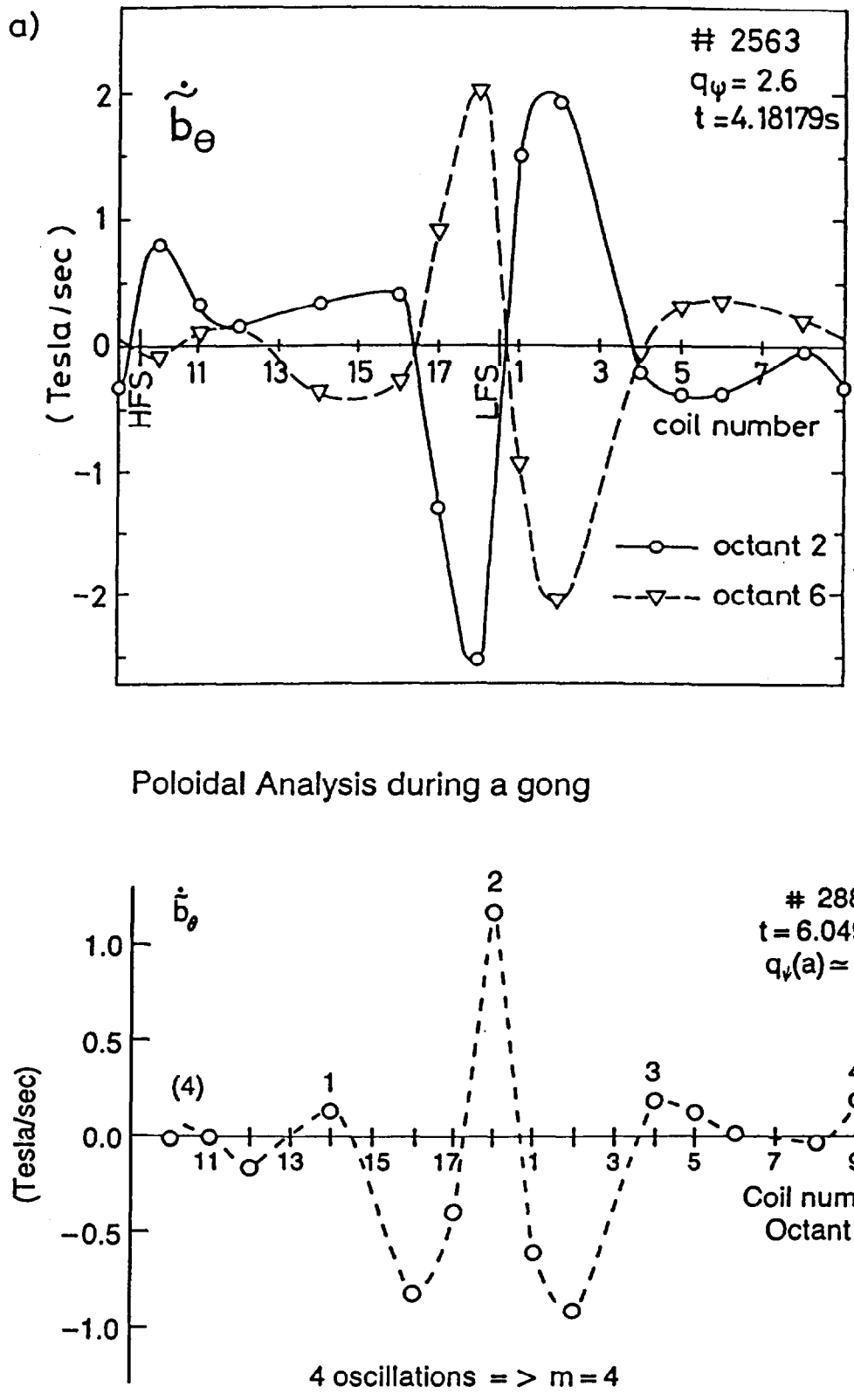

Fig. 7 : Poloidal analysis of the gong ($\tilde{b_\theta}$)
a) Two poloidal arrays located 180° toroidally apart show clearly the dominant n=1 character of the gong, with a remarkable in-out asymmetry. For $q_\psi(a) = 2.6$ the dominant mode appears to be $1<m<3$.
b) For $q_\psi(a) = 4.2$, the dominant mode appears to be m=4.

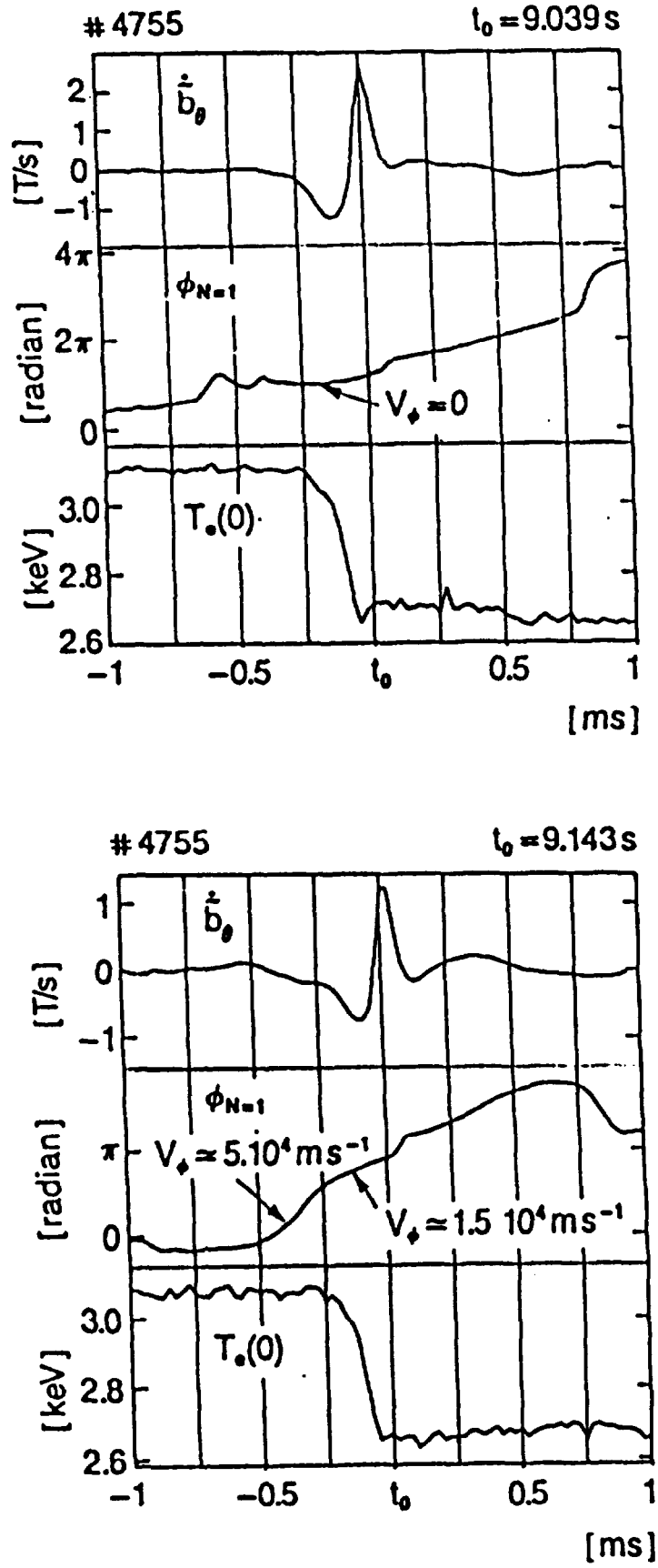

Fig. 8 : Time evolution of n=1 phase showing that the toroidal rotation can be different for two successive gongs belonging to the same discharge.

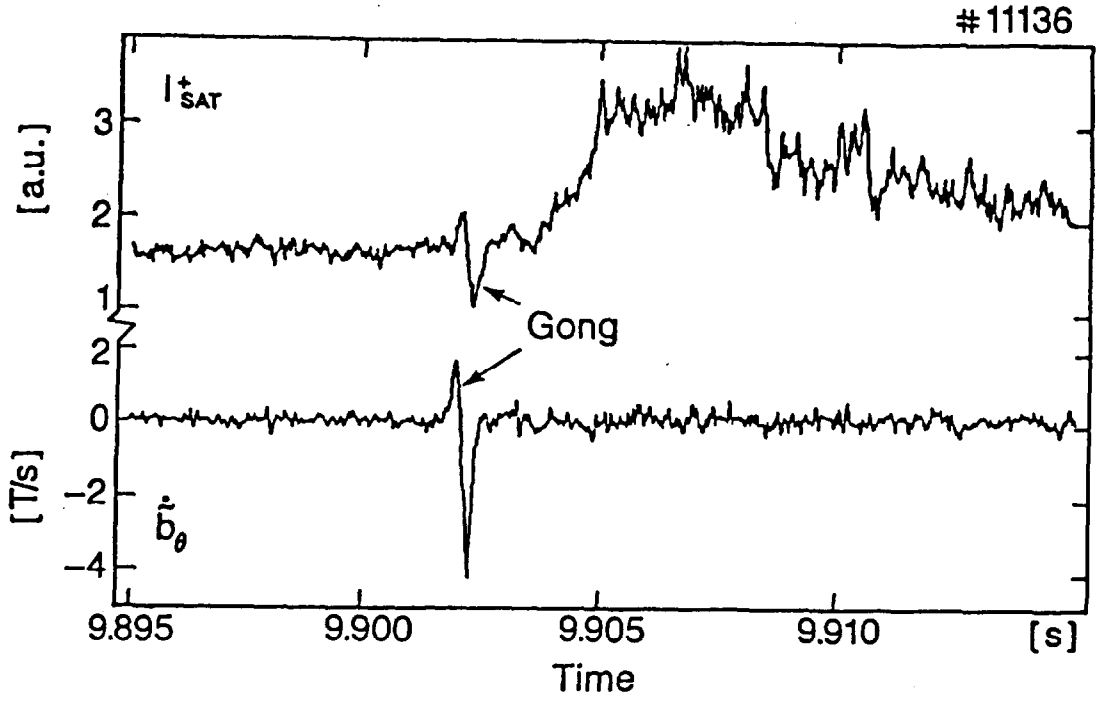

Fig. 9 : The gong can also be observed on an edge Langmuir probe. (The Langmuir probe is located at 4mm from the last closed magnetic surface, on the LFS).

Gong and Centroid Shift

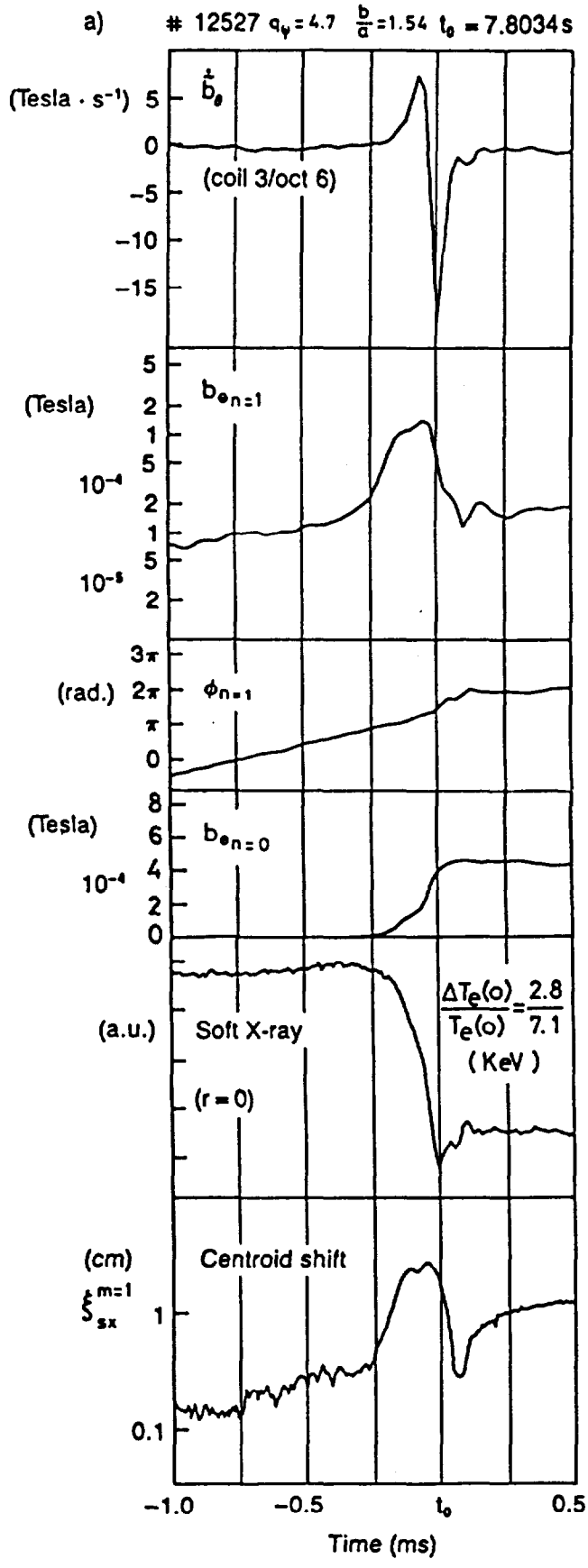

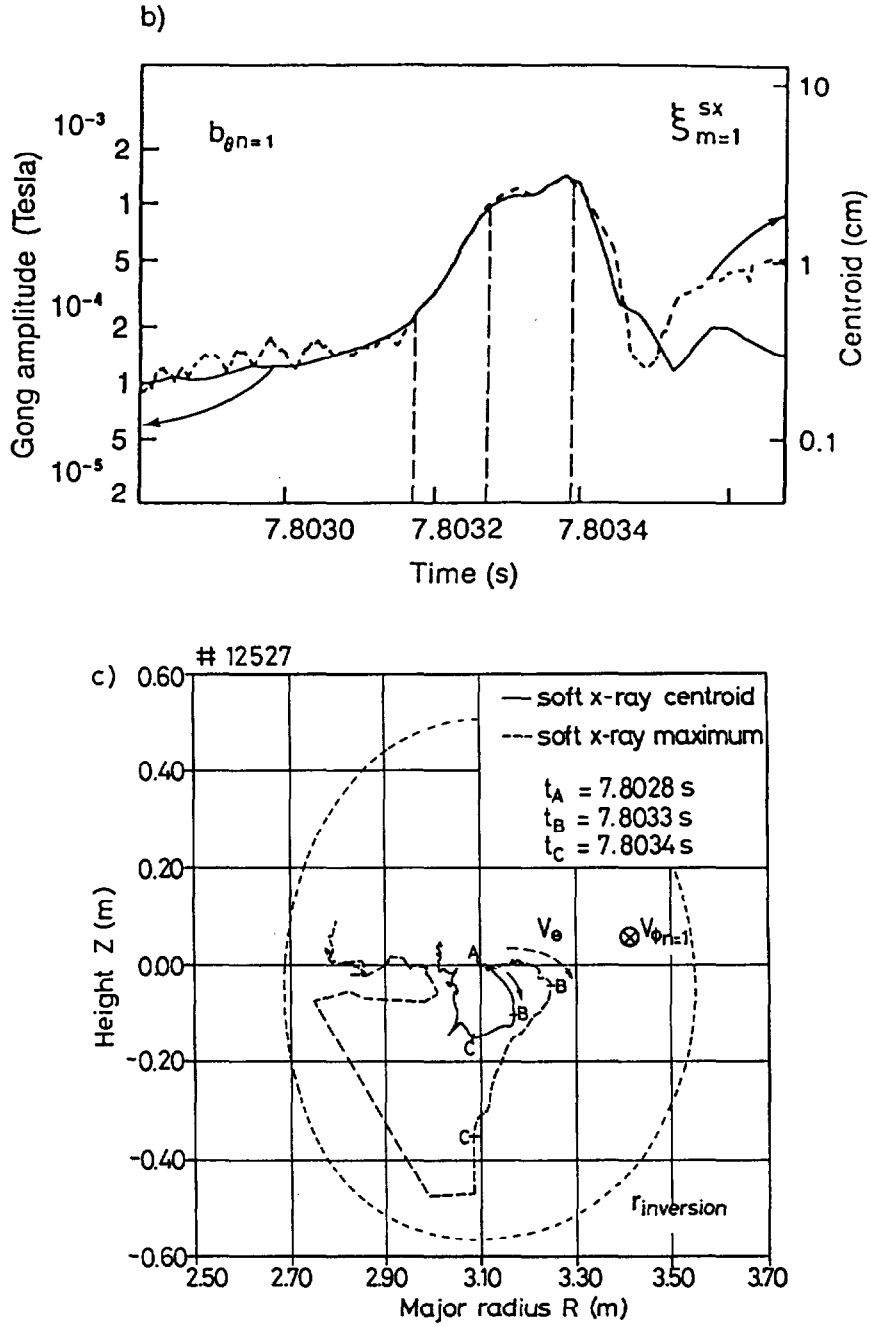

Fig. 10 : Comparison of the gong amplitude and central displacement calculated with the centroid shift, integrated over the full soft X–ray profile.

a) Time evolution of the different traces,

b) Overlapping of the gong amplitude and the centroid shift.

c) Motion of the centroid in the poloidal plane, resulting of integration over $r<r_{inv}$ (full line), and position of the maximum emission (doted line). The instablity grows between A and B, and saturates between B and C. The helicity of the gong can be deduced from the comparison between the centroid azimutal motion v_θ (measured with the soft X-rays) and the toroidal gong rotation $v_{\phi\ n=1}$. The resulting direction of the helicity is the same as that of the equilibrium magnetic field.

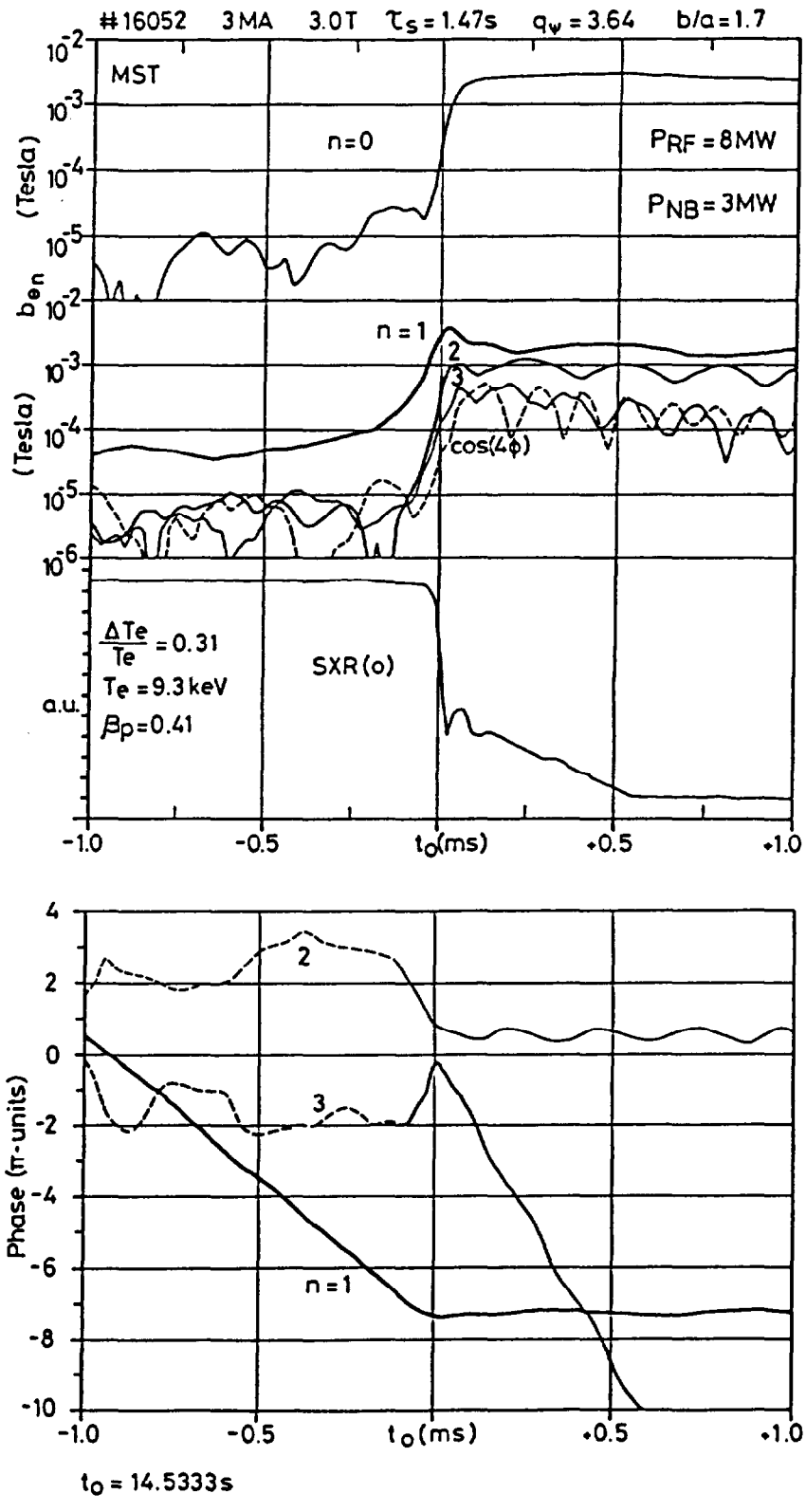

Fig. 11 : Toroidal spectrum of the gong instability for a monster sawtooth (MST). The corresponding phases for the n=1, 2 and 3 modes are also shown in the lower part of the figure.

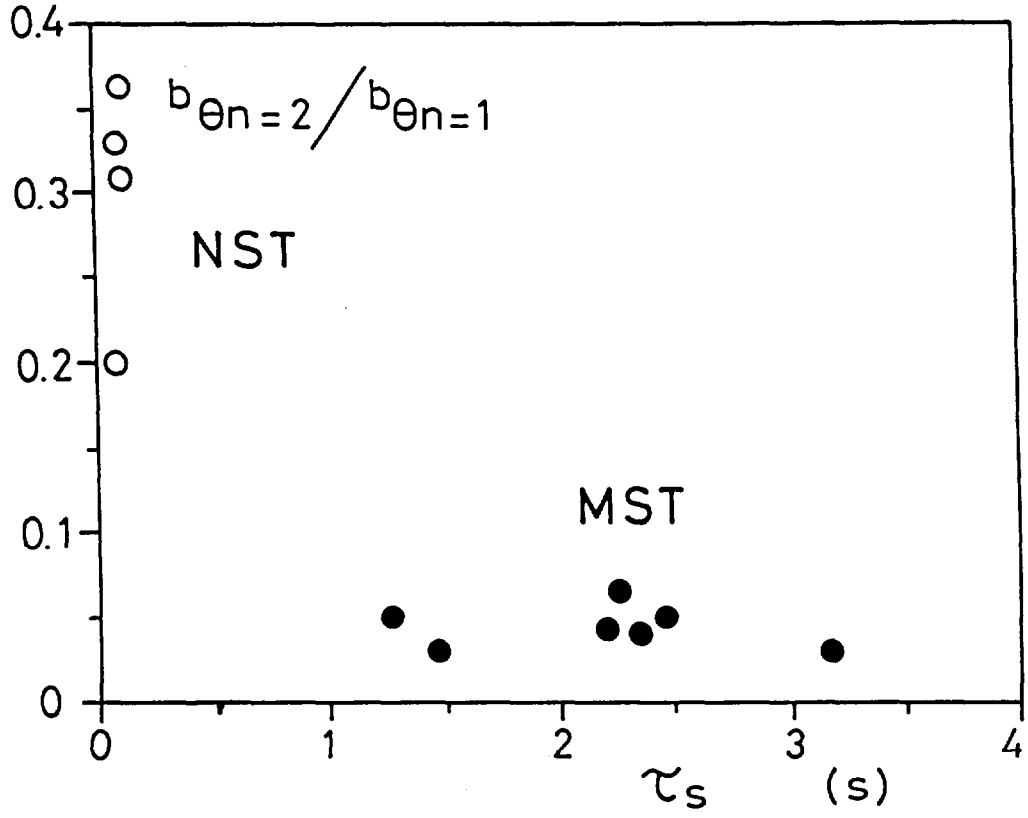

Fig. 12 : Ratio $b_{\theta\, n=2}/b_{\theta\, n=1}$ for NST and MST, depicted as a function of the preceding sawtooth duration.

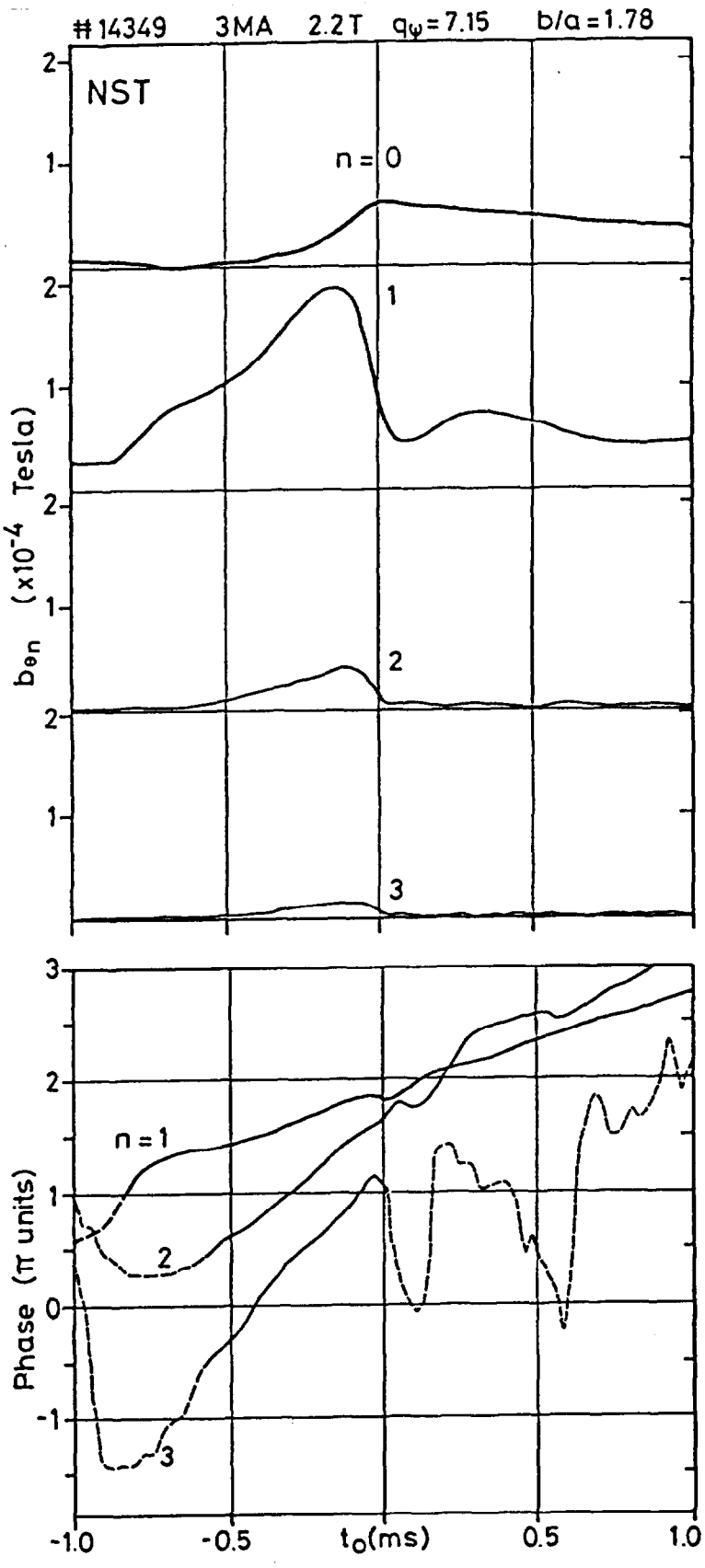

Fig. 13 : Amplitude and toroidal phase for the n=1,2 and 3 components in a NST. The phase plot shows $(\dot{\phi}_{n=1},\dot{\phi}_{n=2},\dot{\phi}_{n=3}) \approx (1,2,3)\cdot\dot{\phi}_{n=1}$ indicative of similar toroidal phase velocities for the different n components : $v_{\phi\, n} \approx v_{\phi\, n=1}$.

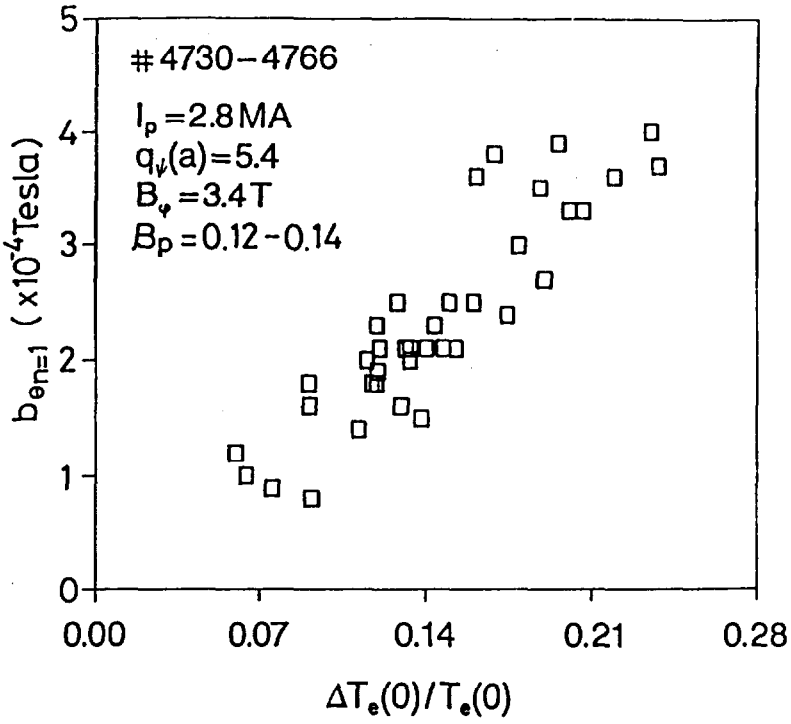

Fig. 14 : Maximum amplitude of $b_{\theta n=1}$(at saturation of the instability) for normal sawteeth versus the normalized central temperature drop $\Delta T_e(0)/T_e(0)$.

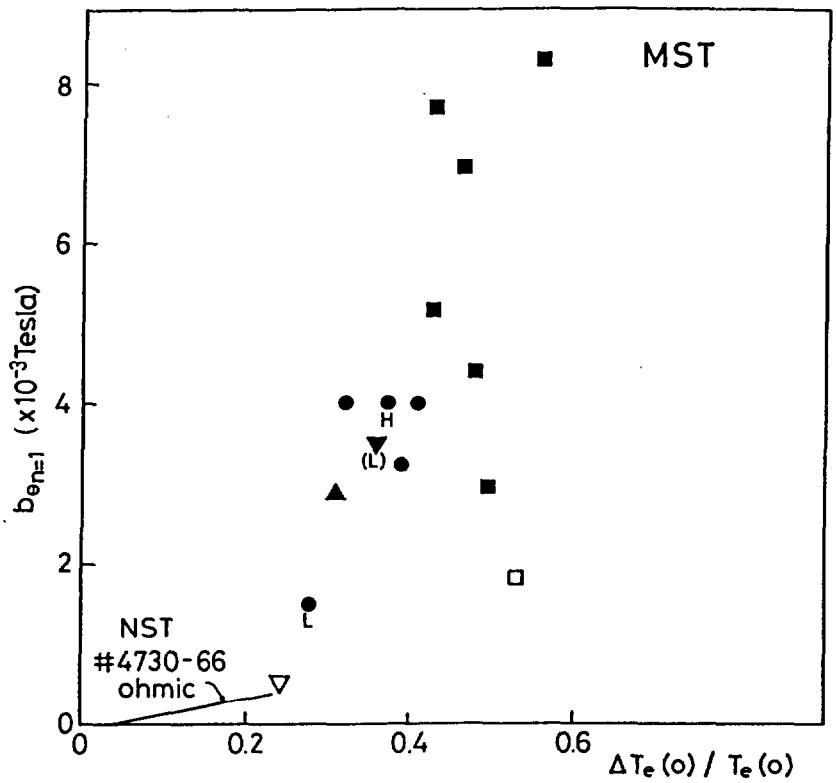

Fig. 15 : Maximum amplitude of $b_{\theta n=1}$ for monster sawteeth versus $\Delta T_e(0)/T_e(0)$. The trend for normal sawteeth is indicated in the left lower corner. Different series of monster sawteeth are indicated by different symbols, see Table I.

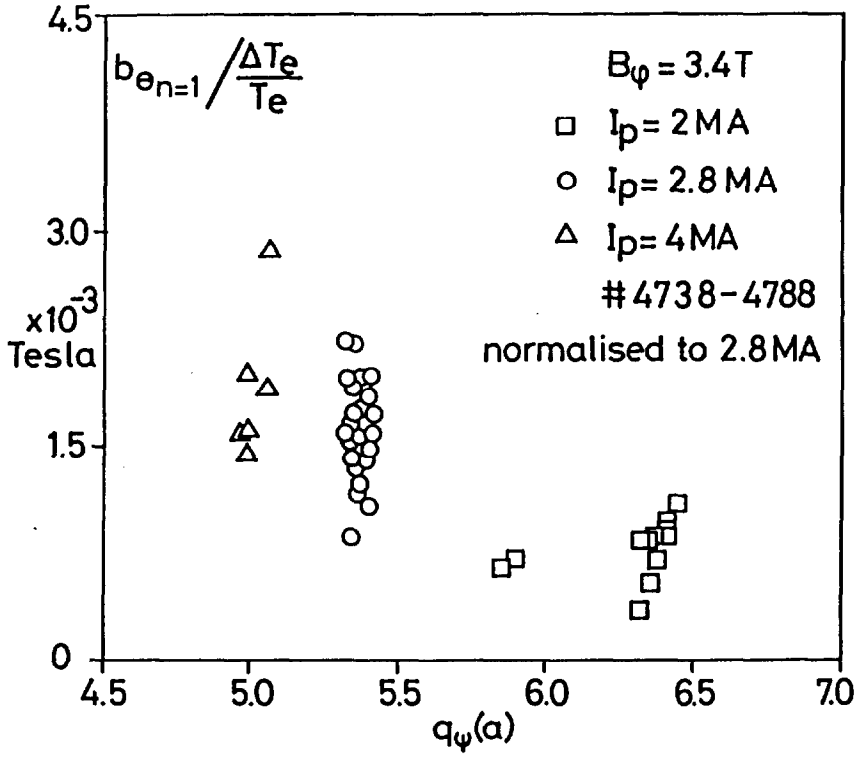

Fig. 16 : The gong amplitude $b_{\theta n=1}$ shown here for normal sawteeth is smaller for larger $q_\psi(a)$. The gong amplitude is both normalized to the relative temperature crash $\Delta T_e(0)/T_e(0)$ and to a plasma current of 2.8 MA.

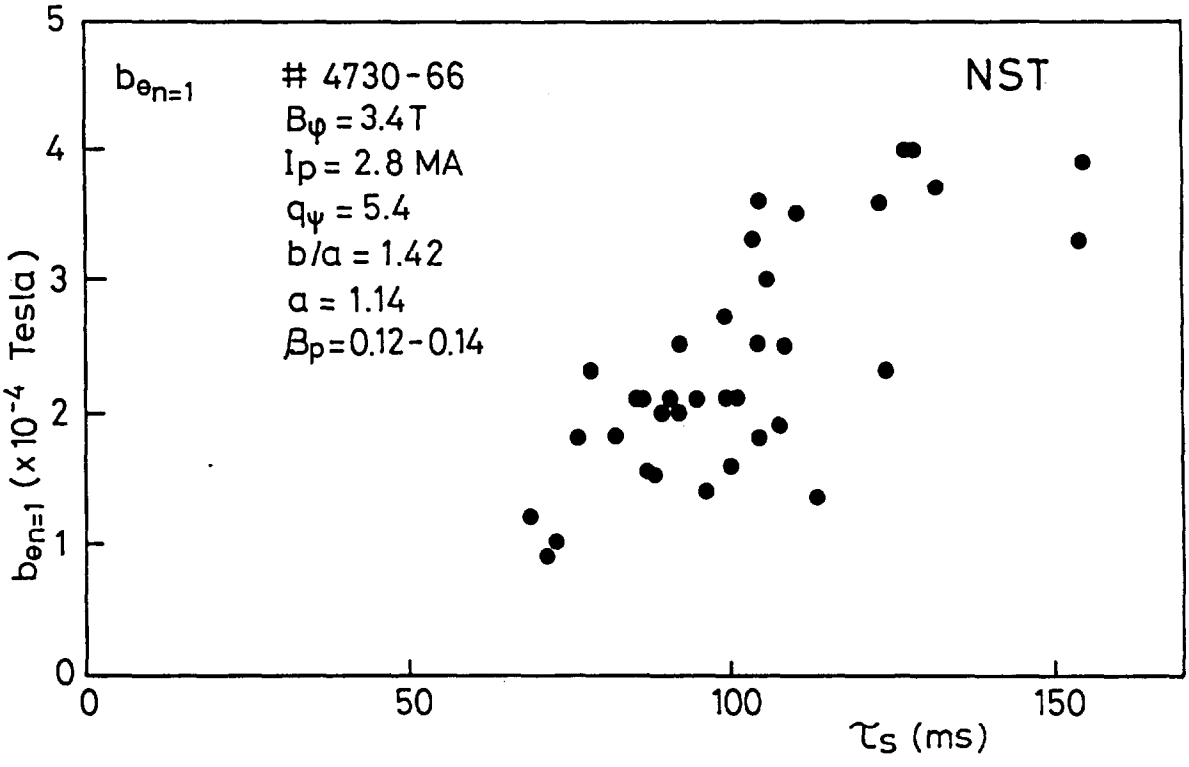

Fig. 17 : The gong amplitude $b_{\theta n=1}$ increases with sawtooth period τ_s for normal sawteeth.

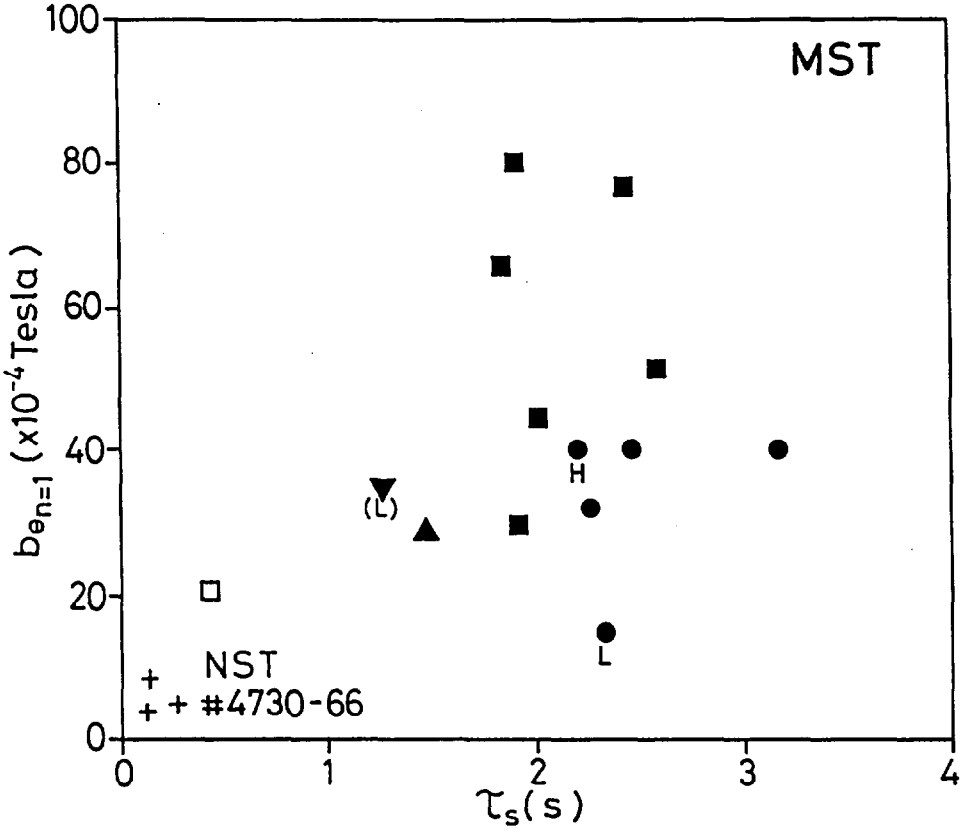

Fig. 18 : The gong amplitude $b_{\theta n=1}$ for monster sawteeth is above the extrapolated value for normal sawteeth (left lower corner) for increasing sawtooth period τ_s. Same data as in Fig. 15, see Table I.

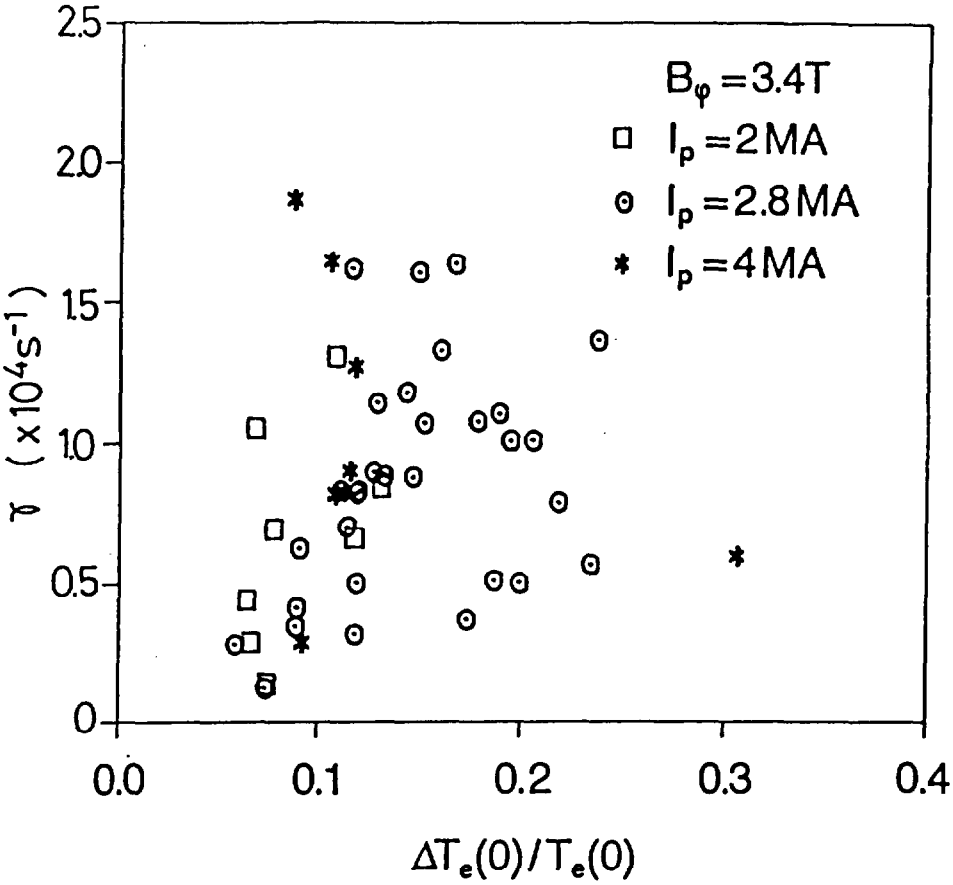

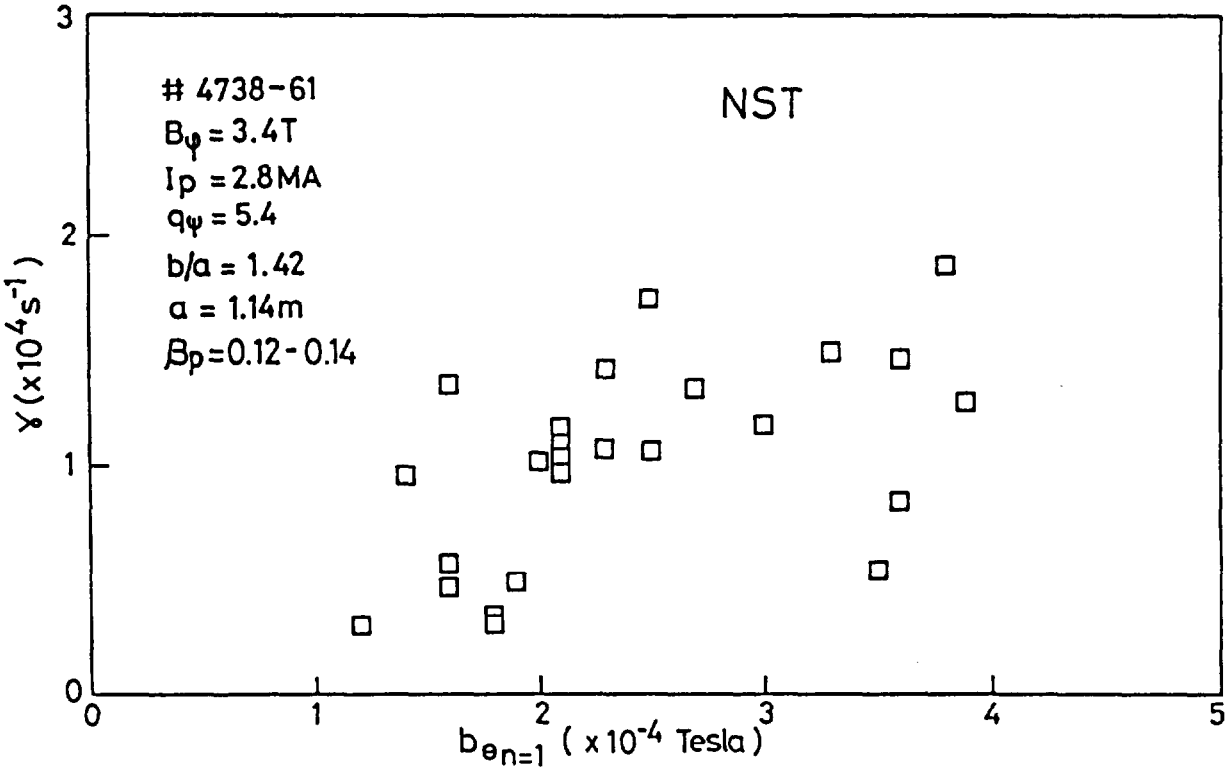

Fig. 19 : a) Growth rates of the instability versus ΔTe(0)/Te for normal sawteeth. No particular trend is visible.

b) Growth rate of the instability versus $b_{\theta n=1}$ for normal sawteeth.

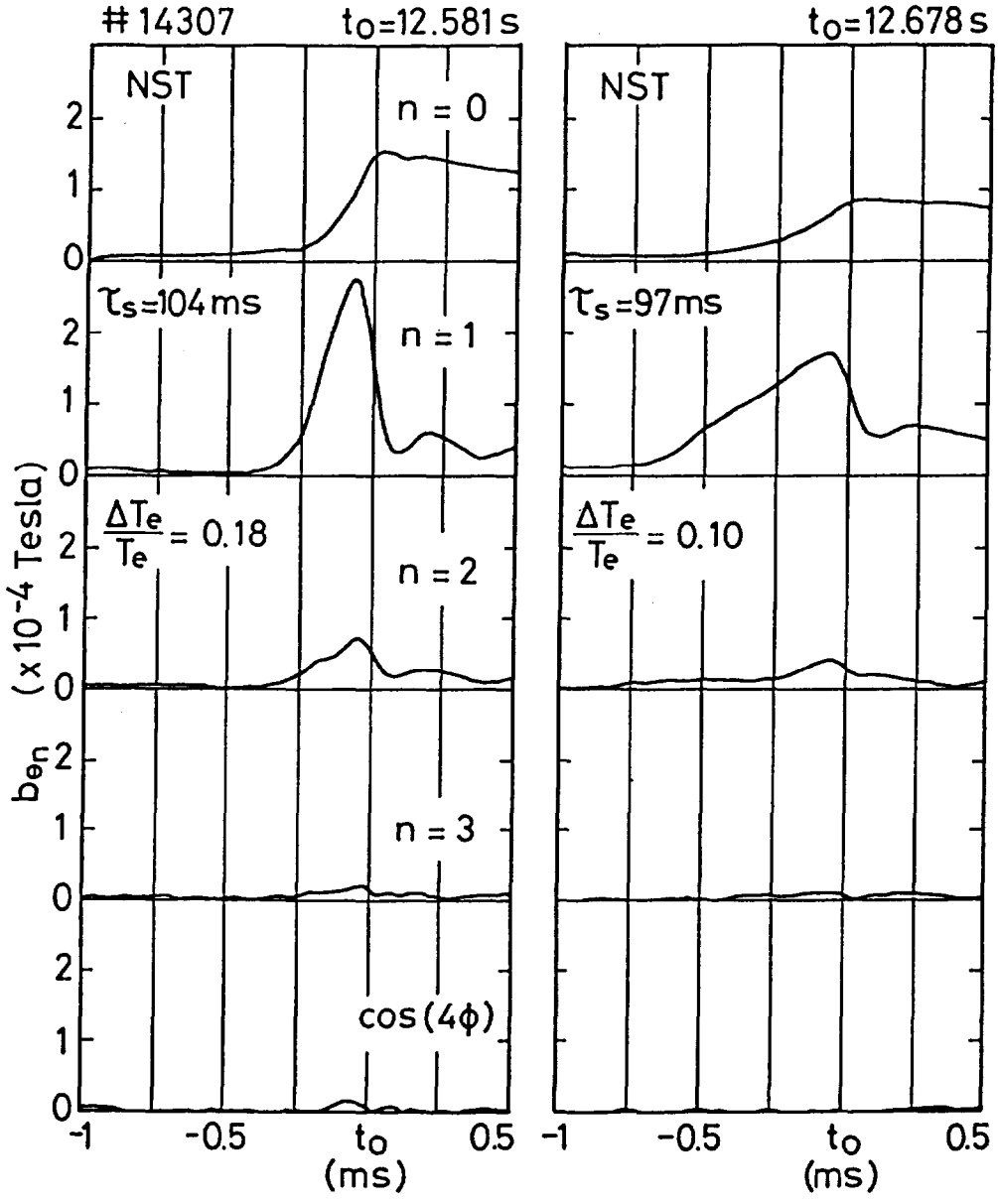

Fig. 20 : Two consecutive sawteeth can show growth rates varying by more than half an order of magnitude in normal sawteeth.

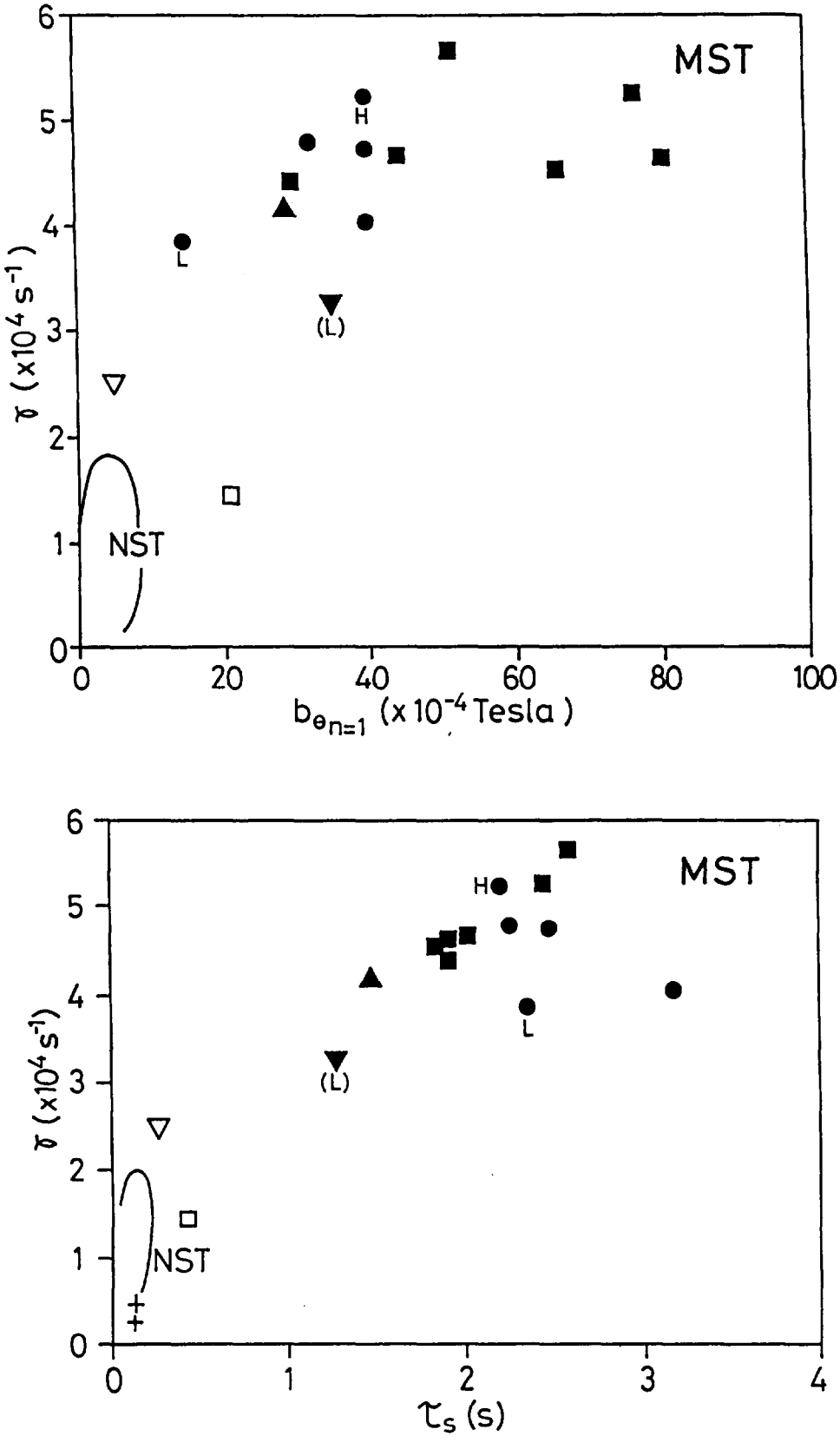

Fig. 21 : a) Growth rate of the instability versus the $b_{\theta n=1}$ component for monster sawteeth.
b) Growth rate versus sawtooth period τ_s. Same data as in Fig. 15 and 18, see Table I.
The trends for normal sawteeth are indicated in the left lower corners.

Appendix I

THE JET TEAM

JET Joint Undertaking, Abingdon, Oxon, OX14 3EA, U.K.

J.M. Adams[1], H. Altmann, A. Andersen[14], P. Andrew[18], M. Angelone[29], S.A. Arshad, W. Bailey, P. Ballantyne, B. Balet, P. Barabaschi, R. Barnsley[2], M. Baronian, D.V. Bartlett, A.C. Bell, I. Benfatto[5], G. Benali, H. Bergsaker[11], P. Bertoldi, E. Bertolini, V. Bhatnagar, A.J. Bickley, H. Bindslev[14], T. Bonicelli, S.J. Booth, G. Bosia, M. Botman, D. Boucher, P. Boucquey, P. Breger, H. Brelen, H. Brinkschulte, T. Brown, M. Brusati, T. Budd, M. Bures, T. Businaro, P. Butcher, H. Buttgereit, C. Caldwell-Nichols, D.J. Campbell, P. Card, G. Celentano, C.D. Challis, A.V.Chankin[23], D. Chiron, J. Christiansen, C. Christodoulopoulos, P. Chuilon, R. Claesen, S. Clement, E. Clipsham, J.P. Coad, M. Comiskey[4], S. Conroy, M. Cooke, S. Cooper, J.G. Cordey, W. Core, G. Corrigan, S. Corti, A.E. Costley, G. Cottrell, M. Cox[7], P. Cripwell, H. de Blank[15], H. de Esch, L. de Kock, E. Deksnis, G.B. Denne-Hinnov, G. Deschamps, K.J. Dietz, S.L. Dmitrenko, J. Dobbing, N. Dolgetta, S.E. Dorling, P.G. Doyle, D.F. Düchs, H. Duquenoy, A. Edwards, J. Ehrenberg, A. Ekedahl, T. Elevant[11], S.K. Erents[7], L.G. Eriksson, H. Fajemirokun[12], H. Falter, D. Flory, J. Freiling[15], C. Froger, P. Froissard, K. Fullard, M. Gadeberg, A. Galetsas, D. Gambier, M. Garribba, P. Gaze, R. Giannella, A. Gibson, R.D. Gill, A. Girard, A. Gondhalekar, C. Gormezano, N.A. Gottardi, C. Gowers, B.J. Green, R. Haange, G Haas, A. Haigh, G. Hammett[6], C.J. Hancock, P.J. Harbour, N.C. Hawkes[7], P. Haynes[7], J.L. Hemmerich, T. Hender[7], F.B. Herzog, R.F. Herzog, J. Hoekzema, J. How, M. Huart, L Hughes, T.P. Hughes[4], M. Hugon, M. Huguet, A. Hwang[7], B. Ingram, M. Irving, J. Jacquinot, H. Jaeckel, J.F. Jaeger, G. Janeschitz[13], S. Jankowicz[22], O.N. Jarvis, F. Jensen, E.M. Jones, L.P.D.F. Jones, T.T.C. Jones, J-F. Junger, E. Junique, A. Kaye, B.E. Keen, M. Keilhacker, G.J. Kelly, W. Kerner, R. Konig, A. Konstantellos, M. Kovanen[20], G. Kramer[15], P. Kupschus, R. Lässer, J.R. Last, B. Laundy, L. Lauro-Taroni, K. Lawson[7], M. Lennholm, A. Loarte, R. Lobel, P. Lomas, M. Loughlin, C. Lowry, B. Macklin, G. Maddison[7], G. Magyar, W. Mandl[13], V. Marchese, F. Marcus, J. Mart, E. Martin, R. Martin-Solis[8], P. Massmann, G. McCracken[7], P. Meriguet, P. Miele, S.F. Mills, P. Millward, R. Mohanti[17], P.L. Mondino, A. Montvai[3], S. Moriyama[28], P. Morgan, H. Morsi, G. Murphy, M. Mynarends, R. Myrnäs[16], C. Nardone, F. Nave[21], G. Newbert, M. Newman, P. Nielsen, P. Noll, W. Obert, D. O'Brien, J. O'Rourke, R. Ostrom, M. Ottaviani, M. Pain, F. Paoletti, S. Papastergiou, D. Pasini, A. Peacock, N. Peacock[7], D. Pearson[12], R. Pepe de Silva, G. Perinic, C. Perry, M. Pick, R. Pitts[7], J. Plancoulaine, J-P. Poffé, F. Porcelli, L. Porte[19], R. Prentice, S. Puppin, S. Putvinsko[23], G. Radford[9], T. Raimondi, M.C. Ramos de Andrade, P-H. Rebut, R. Reichle, E. Righi, F. Rimini, D. Robinson[7], A. Rolfe, R.T. Ross, L. Rossi, R. Russ, P. Rutter, H.C. Sack, G. Sadler, G. Saibene, J.L. Salanave, G. Sanazzaro, A. Santagiustina, R. Sartori, C. Sborchia, P. Schild, M. Schmid, G. Schmidt[6], B. Schunke, S.M. Scott, A. Sibley, R. Simonini, A.C.C. Sips, P. Smeulders, R. Stankiewicz[27], M. Stamp, P. Stangeby[18], D.F. Start, C.A. Steed, D. Stork, P.E. Stott, T.E. Stringer, P. Stubberfield, D. Summers, H. Summers[19], L. Svensson, J.A. Tagle[21], A. Tanga, A. Taroni, A. Tesini, P.R. Thomas, E. Thompson, K. Thomsen, J.M. Todd, P. Trevalion, B. Tubbing, F. Tibone, E. Usselmann, H. van der Beken, G. Vlases, M. von Hellermann, T. Wade, C. Walker, R. Walton[6], D. Ward, M.L. Watkins, M.J. Watson, S. Weber[10], J. Wesson, T.J. Wijnands, J. Wilks, D. Wilson, T. Winkel, R. Wolf, B. Wolle[24], D. Wong, C. Woodward, Y. Wu[25], M. Wykes, I.D. Young, L. Zannelli, Y. Zhu[26], W. Zwingmann.

PERMANENT ADDRESSES

1. UKAEA, Harwell, Didcot, Oxon, UK.
2. University of Leicester, Leicester, UK.
3. Central Research Institute for Physics, Academy of Sciences, Budapest, Hungary.
4. University of Essex, Colchester, UK.
5. ENEA-CNR, Padova, Italy.
6. Princeton Plasma Physics Laboratory, New Jersey, USA.
7. UKAEA Culham Laboratory, Abingdon, Oxon, UK.
8. Universidad Complutense de Madrid, Spain.
9. Institute of Mathematics, University of Oxford, UK.
10. Freien Universität, Berlin, F.R.G.
11. Swedish Energy Research Commission, S-10072 Stockholm, Sweden.
12. Imperial College of Science and Technology, University of London, UK.
13. Max Planck Institut für Plasmaphysik, Garching bei München, FRG.
14. Risø National Laboratory, Denmark.
15. FOM Instituut voor Plasmafysica, 3430 Be Nieuwegein, The Netherlands.
16. University of Lund, Sweden.
17. North Carolina State University, Raleigh, NC, USA
18. Institute for Aerospace Studies, University of Toronto, Downsview, Ontario, Canada.
19. University of Strathclyde, 107 Rottenrow, Glasgow, UK.
20. Nuclear Engineering Laboratory, Lapeenranta University, Finland.
21. CIEMAT, Madrid, Spain.
22. Institute for Nuclear Studies, Otwock-Swierk, Poland.
23. Kurchatov Institute of Atomic Energy, Moscow, USSR
24. University of Heidelberg, Heidelberg, FRG.
25. Institute for Mechanics, Academia Sinica, Beijing, P.R. China.
26. Southwestern University of Physics, Leshan, P.R. China.
27. RCC Cyfronet, Otwock Swierk, Poland.
28. JAERI, Naka Fusion Research Establishment, Ibaraki, Japan.
29. ENEA, Frascati, Italy.

At 1st June 1991